ELSEVIER

Chemical Engineering Science 62 (2007) 4620–4635

Chemical Engineering Science

www.elsevier.com/locate/ces

Simulation of nanotube separation in field-flow fractionation (FFF)☆

Frederick R. Phelan Jr.*, Barry J. Bauer

Polymers Division, NIST, Gaithersburg, MD 20899, USA

Received 30 September 2006; received in revised form 13 April 2007; accepted 14 April 2007
Available online 29 April 2007

Abstract

A Brownian dynamics simulation based on a prolate spheroid particle model has been developed to model the separation of nanotubes in cross flow driven, field-flow fractionation (FFF). The particle motions are governed by stochastic forms of a linear momentum balance with orientation dependent drag and diffusion coefficients, and the Jeffrey equation with rotational diffusion. The simulation shows that nanotube scale particles would be expected to elute by a normal mode mechanism up to aspect ratios of about 1000, based on a particle diameter of 1 nm. Separation of nanotubes of different length is governed by the value of the retention variable for each component in agreement with theory. Elution profiles and average velocity through the device as a function of particle size, and the flow rates in the throughput and cross-flow directions are examined. The simulation shows that clean separations between components of different size is achieved when the ratio of the retention values is greater than 2.
Published by Elsevier Ltd.

Keywords: Brownian dynamics; Flow-field fractionation; Jeffrey equation; Nanotubes; Separations; SWNT

1. Introduction

The manufacturing of single wall carbon nanotubes (SWNTs) results in mixtures that are polydisperse with respect to both size and chirality,[1] the latter of which strongly affects the tube electronic properties.[2] For nanotube properties to be fully understood scientifically and to achieve their full potential in applications, it is desirable to be able to separate them according to both of these physical characteristics. A number of recent works addressing both these issues have emerged and Haddon et al. (2004) and Krupke and Hennrich (2005) have discussed many of these in their reviews. Length-based separation techniques include size exclusion chromatography (SEC) (Duesberg et al., 1998, 1999; Chattopadhyay et al., 2002; Farkas et al., 2002; Huang et al., 2005; Yang et al., 2005; Arnold et al., 2006a), field-flow fractionation (Chen and Selegue, 2002; Moon et al., 2004; Selegue et al., 2001; Tagmatarchis et al., 2005; Peng et al., 2006; Liu et al., 1998), and various forms of electrophoresis (Doorn et al., 2003; Suarez et al., 2006; Vetcher et al., 2006). Chiral-based separation techniques include dieloectrophoresis (Peng et al., 2006; Krupke et al., 2003; Banerjee et al., 2005; Hennrich et al., 2005; Chen et al., 2006), ion-exchange chromatography (Zheng et al., 2003a,b), centrifugation (Maeda et al., 2005, 2006; Arnold et al., 2006b), and a variety of methods involving chemical selectivity, dissolution, or functionalization (sometimes in combination with other techniques) (Strano et al., 2003; Chattopadhyay et al., 2003; Chen et al., 2003; Samsonidze et al., 2004; Toyoda et al., 2007). As an example of an application of such techniques, biotoxicity has been measured as a function of SWNT length from (50 to 500) nm using size exclusion chromatography (SEC) to produce the length fractions (Becker et al., 2007) using the SEC profile developed by Huang et al. (2005).

Field-flow fractionation (FFF) (Giddings, 1993, 2000; Janca, 1987) is a liquid based technique used to separate various

☆ Official contribution of the National Institute of Standards and Technology; not subject to copyright in the United States.

* Corresponding author. Tel.: +1 301 975 6761; fax: +1 301 975 4924.
E-mail address: frederick.phelan@nist.gov (F.R. Phelan Jr.).

[1] A carbon nanotube is like a cylinder rolled up from a single sheet of graphite, whose atoms are arranged in hexagons. Rolling the lattice at different angles creates a visible twist or spiral in the nanotube's molecular structure. This twist is called chirality.

[2] e.g., http://www.ncnr.nist.gov/staff/taner/nanotube/types.html. For a given (n, m) nanotube, if $2n + m = 3q$ (where q is an integer), then the nanotube is metallic, otherwise the nanotube is a semiconductor.

0009-2509/$ - see front matter Published by Elsevier Ltd.
doi:10.1016/j.ces.2007.04.019

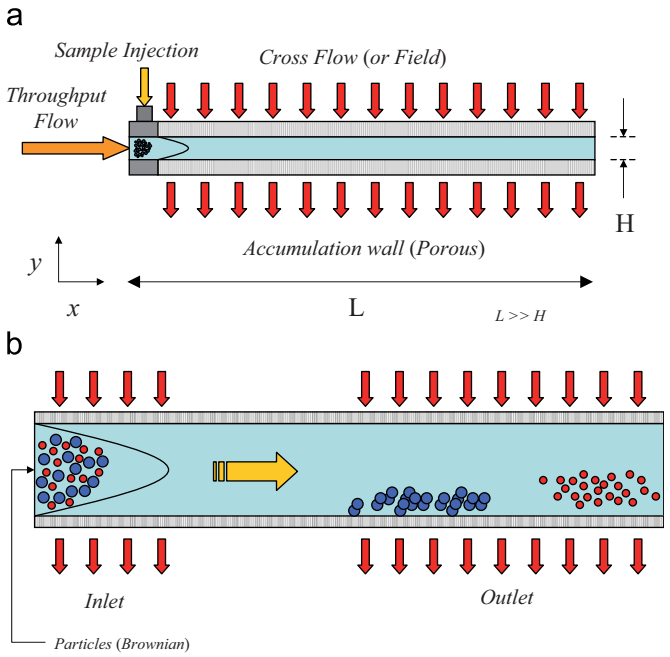

Fig. 1. (a) The frit inlet symmetrical variation (FIS-FFF) of classical flow-FFF. The cross flow is achieved through the use of porous membranes along the upper and lower channels. The lower wall is called the Accumulation wall as particles tend to be driven towards (but not into) this boundary. (b) Separation is achieved due to the different residence times of the particles based upon their average equilibrium position in the parabolic velocity profile as they travel in the throughput direction.

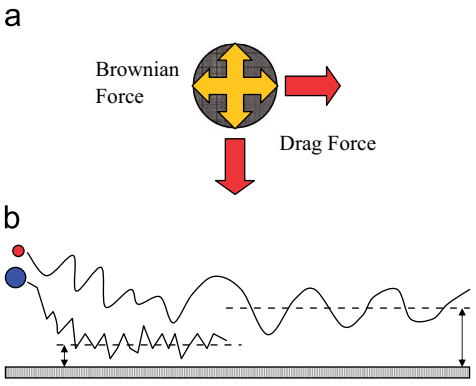

Fig. 2. (a) Forces acting on a particle in flow-FFF. (b) In normal mode FFF, smaller particles which are more diffusive and experience less drag, have an average position closer to the centerline.

macromolecular, colloidal, and particulate materials ranging from 10^{-3} to 10^{2} μm in size and as mentioned has recently been applied in a number of studies (Chen and Selegue, 2002; Moon et al., 2004; Selegue et al., 2001; Tagmatarchis et al., 2005; Peng et al., 2006; Liu et al., 1998) to the separation of nanotubes. FFF has several advantages over other separation methods in length-based separations including a wider size range over which separations can be produced, as well as the ability to separate clusters from individually dispersed SWNTs (which would clog an SEC column). In addition, FFF can be combined with other techniques such as dielectrophoresis (Peng et al., 2006) to produce chiral based separations. In this work, we seek to develop a model for simulating the nanotube separation process in FFF based on tube size and processing parameters.

In FFF, a mixture to be separated is driven through a channel (the "flow", in FFF) while a field is applied in a direction perpendicular to the streamwise direction. The perpendicular field may be a second flow field, an electric field, or a temperature gradient, amongst a number of possibilities. The perpendicular field is chosen so that the interaction between the field and the streamwise parabolic velocity profile promotes a separation of components based on their mobility in the field. The frit inlet symmetrical variation (FIS-FFF) of classical flow-FFF is shown in Fig. 1a. The mixture to be separated is injected into the channel and a cross flow is imposed upon the throughput flow driving the particulates towards the lower boundary (called accumulation wall). The cross flow is achieved through the use of porous membranes along the upper and lower channel boundaries that allow flow of the solvent, but which are impermeable to the particulates. The flow rates in the throughput and cross flow directions are independently varied by means of pressure controllers to manipulate the rate at which particles traverse the system, and to control how closely particles of different size approach the accumulation wall (without embedding), respectively. Separation is achieved due to the different residence times of the particles based upon their average equilibrium position in the parabolic velocity profile as shown in Fig. 1b—particles which travel closer to the center elute more quickly than those closer to the wall. In practice, the length, L, of the flow channel is much greater than the gap width, H. Gap widths on the order of 100–500 μm are typically used although gaps as small as 10 μm have also been reported (Giddings, 1993). The process may be optimized in a number of ways. The throughput channel may be tapered in the third direction to further accelerate faster moving particles. Programmable cross flow rates can go to zero through a ramp or step function to allow slower moving particles to elute more quickly once fast movers have exited.

A number of different mechanisms can be exploited to achieve separation in flow-FFF (Giddings, 1993, 2000; Janca, 1987). What is termed normal mode separation applies to particles that are small enough to undergo significant Brownian motion and are much smaller than the size scale of the channel, which is the case for nanotubes. Because the solutions are dilute, the main forces acting on the particles are the drag force and the Brownian force, as shown in Fig. 2a. Under these conditions, smaller particles which are more diffusive and experience less drag, travel with an average position closer to the centerline and thus on average move more quickly downstream as pictured in Fig. 2b. For an ensemble of particles, this competition between streamwise advection and diffusion in the cross-flow direction drives particles of different sizes to discrete equilibrium layers and positions. The particle "clouds" are characterized by their average horizontal spread along the throughput direction, Δx, and their average position from the accumulation wall, Δy, as depicted in Fig. 3. Clean separations are achieved when particle clouds of different type do

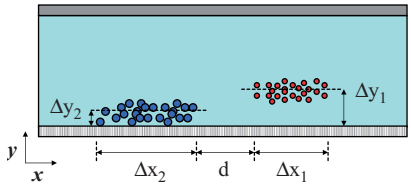

Fig. 3. Characteristic particle "clouds" in flow-FFF. Clouds are characterized by their average horizontal spread in the throughput direction, Δx, and their average distance above the lower surface, Δx. It is desirable to choose the processing parameters such that particle clouds of different type do not overlap.

not overlap, and a separation distance d is achieved between the horizontal positions of the layers.

The process of separation in normal mode flow-FFF can be characterized by the theoretical variable called the retention, which is given by

$$R = \frac{\overline{U}}{\overline{u}} = \frac{\langle c(y)U(y)\rangle}{\langle c(y)\rangle\langle u(y)\rangle}, \tag{1}$$

where $\overline{U}$ is the average streamwise velocity of the solute, c is the concentration of the solute, $\overline{u}$ is the average streamwise velocity of the carrier fluid, and the brackets $\langle\ldots\rangle$ represent the integral average over the flow cross section. The retention is significant because it represents the ratio of the average residence time of non-retained tracers, t_0, to the average retention time of the particles, t_r. This is expressed by the relationship

$$\frac{t_r}{t_0} = \frac{1}{R}, \tag{2}$$

where $t_0 = L/\overline{u}$.

The competition between advection and diffusion in the cross-flow direction leads particles to an equilibrium concentration profile in the gap direction given by

$$\frac{c}{c_0} = \exp\left(-\frac{y}{\ell}\right), \tag{3}$$

where c_0 is the concentration of the particles at the accumulation wall, ℓ is a characteristic length given by

$$\ell = \frac{D}{|v_c|}, \tag{4}$$

where v_c is the cross-flow velocity, and D is the diffusion coefficient of the particle in the cross-flow direction. Assuming a parabolic velocity profile for flow in the throughput direction and that the value for $|v_c|$ is constant, Eq. (1) can be integrated to yield an analytical relation for the retention given by

$$R = 6\lambda\left[\coth\left(\frac{1}{2\lambda}\right) - 2\lambda\right], \tag{5}$$

where λ is an inverse Peclet Number (Pe) given by

$$\lambda = \frac{D}{|v_c|H} = \frac{1}{Pe}. \tag{6}$$

The retention is a dimensionless variable whose value is bounded in the range $0 < R < 1$. In the limit $R = 0$, particles are trapped on the accumulation wall, and thus, this corresponds to the case of zero elution. As R increases, the average speed at which particles elute also increases approaching the minimum t_0 at $R = 1$. Thus, the ability to separate particles depends on the relative retention values of the different particles dispersed in the solution.

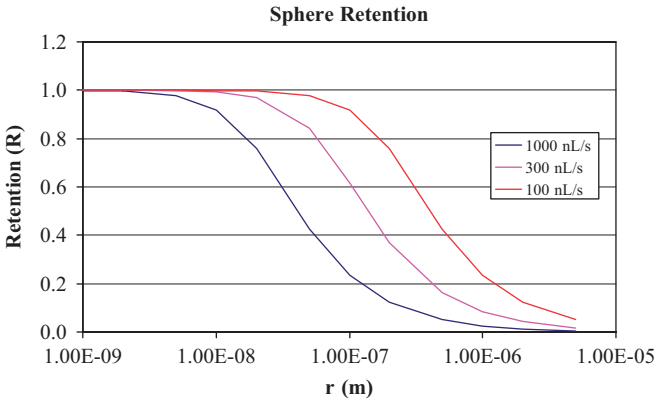

Fig. 4. A plot of the retention variable for spherical particles under typical conditions in flow-FFF.

Table 1
Typical conditions for conducting separations in flow-FFF

L (m)	W (m)	H (mm)	Viscosity (Pa-s)	Temperature (K)
0.2	0.01	0.1	0.001	293

For spherical particles the diffusion coefficient is given by $D = kT/\zeta$ where $\zeta = 6\pi r\eta$ is the Stokes' law drag coefficient, r is the radius of the particle, η is the viscosity of the fluid, k is Boltzmann's constant, and T is the absolute temperature. A plot of the retention for spheres across a distribution of sizes is shown in Fig. 4 using some typical operating conditions for FFF given in Table 1. The sigmoidal shape of the curves and the shifting of the curves with respect to the cross flow flowrate is significant. For example, the difference in retention between particles with radii 10^{-7} and 10^{-6} m is very small at a flowrate of 1000 nL/s, but quite large at a flowrate of 100 nL/s. Thus, determining retention curves for nanotubes and what sort of different retention differences lead to clean separations for tubes is an important goal of the modeling.

There is a large body of previous work modeling the behavior of fibers suspended in fluid flow that can be applied to the development of a simulation for flow-FFF. Flow models for fibers may be roughly divided into two categories, rigid rod models in which treat the fiber as a single inflexible particle (Satoh, 2003; Kim and Karrila, 1991; Ausias et al., 2006; Cobb and Byron, 2005; Cobb and Butler, 2006; Butler and Shaqfeh, 2005, 2002; Dhont and Briels, 2003; Dhont et al., 1999; Tao et al. 2006, 2005a, b; Mackaplow and Shaqfeh, 1996; Saintillan et al., 2005), and bead-rod or hinged rod type models which allow for some flexibility in the fiber (Montesi et al., 2005; Hsieh et al., 2006; Klaveness and Elgsaeter, 1999; Ross and Klingenberg, 1998; Schmid et al., 2000; Schmid and Klingenberg, 2000a, b;

Skjetne et al., 1997; Switzer and Klingenberg, 2003; Tang and Advani, 2005;Yamamoto and Matsuoka, 1993; 1995a, b; 1996; 1997; Perrin, 1936; Jeffery, 1922). Models may be further subdivided as particle level or continuum, Brownian or non-Brownian motion, and those which include either hydrodynamic interactions or excluded volume effects (Ausias et al., 2006; Cobb and Byron, 2005). The two most fundamental factors to take into account in a flow-FFF process model are the high aspect ratio of the particles and Brownian motion, as the process depends critically upon diffusion. Separations in flow-FFF are usually conducted with very dilute, aqueous solutions, in which it can be assumed that the tubes do not interact. Under these conditions it is reasonable to assume Newtonian solution rheology, and that effects from fiber flexibility and excluded volume interactions are negligible. In addition, because the aspect ratio of the particles is large (in addition to the solutions being dilute), hydrodynamic interactions may be neglected as well (Dhont and Briels, 2003).

In what follows, we develop a particle level simulation to model the behavior of nanotubes in classical flow-FFF. The nanotubes are modeled as a dilute solution of ellipsoidal (prolate spheroid) particles with Brownian motion. The particle motions are governed by stochastic forms of a linear momentum balance with orientation dependent drag and diffusion coefficients, and the Jeffery equation with rotational diffusion (Satoh, 2003; Kim and Karrila, 1991). The paper is organized as follows. In the modeling section, we review the theory for the advection of particles in fluid flow and use that to develop a general model for the flow of dilute ellipsoids with Brownian motion. The specific equation set used to model flow-FFF based on the kinematics of that process is derived, along with a description of the numerical procedures. In the results section, we first verify the simulation model and procedures by comparing numerical results with theoretical results for pure diffusion and the Jeffery's equation in the absence of Brownian motion. We also briefly compare the behavior or Jeffery's equation under both Brownian and non-Brownian conditions. We then analyze the elution process for a monodisperse system in flow-FFF and characterize the dispersion process (streamwise) and the formation of the characteristic particle clouds. Finally, we compute elution profiles across a range of particle sizes, and show that clean separations can be achieved by varying processing parameters so that competing fractions have the correct minimum ratio of retention values. In the Discussion, we further analyze the results in regard to retention ratios, and discuss the possibility of applying FFF methods to the separation of tubes based on chirality.

2. Brownian dynamics simulation

2.1. Advection of particles in viscous flow

The motion of a particle immersed in a flowing liquid is governed by two equations, conservation of linear momentum (Newton's second law) and conservation of angular momentum. In the context of the present work, the two most basic forces that act on the particle are drag forces which arise due to the action of the stress in the fluid on the particle, and the random Brownian force, which arises due to the molecular motion of the fluid on the particle. In terms of these forces, the respective conservation equations may be written without loss of generality as

$$m\frac{\mathrm{d}\underline{U}}{\mathrm{d}t} = -\underline{F}_D(t) + \underline{F}_B(t) + \sum_j \underline{F}_{\{j\}}, \tag{7}$$

$$\underline{\underline{M}} \cdot \frac{\mathrm{d}\underline{\Omega}}{\mathrm{d}t} = -\underline{\mathrm{T}}_D(t) + \underline{\mathrm{T}}_B(t) + \sum_j \underline{\mathrm{T}}_{\{j\}}, \tag{8}$$

where m is the mass of the particle, $\underline{\underline{M}}$ is the moment of inertia tensor, $\underline{U}$ is the velocity of the particle, $\underline{\Omega}$ is the angular momentum of the particle, $\underline{F}_D(t)$ is the fluid-particle drag force, $\underline{F}_B(t)$ is a random force due to Brownian motion, $\underline{\mathrm{T}}_D(t)$ is a drag induced torque, $\underline{\mathrm{T}}_B(t)$ is a random torque due to Brownian motion, and $\sum_j \underline{F}_{\{j\}}$ and $\sum_j \underline{\mathrm{T}}_{\{j\}}$ represent other forces and torques acting on the particle.

The solution of these equations is in some way related to solution of the fluid dynamics problem, either via the flow kinematics or via coupling with the momentum balance for the fluid (generally, the Navier–Stokes equations). The drag force, torque and also the stress exerted by the particle on the ambient fluid may be evaluated in terms of the fluid stress, and are given by

$$\underline{F}_D = -\int_{S_p} (\hat{n} \cdot \underline{\underline{\tau}})\,\mathrm{d}S, \tag{9}$$

$$\underline{\mathrm{T}}_D = -\int_{S_p} (\underline{r} - \underline{r}_c) \times (\hat{n} \cdot \underline{\underline{\tau}})\,\mathrm{d}S, \tag{10}$$

$$\underline{\underline{S}} = -\frac{1}{2}\int_{S_p} \left\{ (\underline{r} - \underline{r}_c)(\hat{n} \cdot \underline{\underline{\tau}}) + (\hat{n} \cdot \underline{\underline{\tau}})(\underline{r} - \underline{r}_c) - \frac{2}{3}(\hat{n} \cdot \underline{\underline{\tau}}) \cdot (\underline{r} - \underline{r}_c)\underline{\underline{I}} \right\} \mathrm{d}S, \tag{11}$$

where $\underline{\underline{\tau}}$ is the stress tensor of the fluid, $\hat{n}$ is the unit normal vector directed outwardly from the surface, S_p denotes the surface of the particle, and $\underline{r}_c$ is the position vector of the particle at its center of mass. The quantity $\underline{\underline{S}}$ is called the stresslet. Analytical relationships for drag force, torque and the stresslet for different particle types are given in a number of references (Satoh, 2003; Kim and Karrila, 1991).

When the concentration of particles in a fluid is dilute, the forces and torques given by Eqs. (9)–(10) do not significantly alter the flow field, and the motion of the particles governed by Eqs. (7)–(8) may be calculated independently of the momentum balance for the fluid assuming the kinematics are known. However, when the particles are of sufficient concentration, the flow field is altered. This couples Eqs. (7)–(8) with the solution for the motion of the fluid. In this case, the stresslet must be incorporated into the momentum balance for the fluid in order to obtain a solution to the problem.

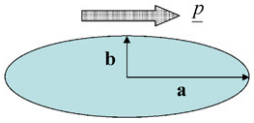

Fig. 5. Model parameters and orientation vector for the prolate spheroid.

2.2. Model for ellipsoidal particles (prolate spheroids)

Since separations in flow-FFF are usually conducted with very dilute, aqueous solutions, as mentioned, in developing a process model we make the assumptions of Newtonian solvent rheology and negligible excluded volume effects. Hydrodynamic interactions are neglected as well (Dhont and Briels, 2003) due to the large particle aspect ratios. To model the drag force generated by the particles in the flow, the nanotubes are modeled as a class of ellipsoids called prolate spheroids (Satoh, 2003; Kim and Karrila, 1991), shown in Fig. 5. A prolate spheroid is formed by the rotation of an ellipse about its major axis. The object has a major axis of length, $2a$, a minor axis of length, $2b$, and is symmetric to the minor axis in the third direction. The orientation vector $\underline{p}$ describes the direction of the major axis in 3-D space. The eccentricity of the ellipsoid is given by the equation

$$s = \frac{\sqrt{a^2 - b^2}}{a}. \tag{12}$$

Because the particles rotate in the flow, the drag force is orientation dependant. The drag force for an ensemble of particles is described by the relation (Satoh, 2003; Kim and Karrila, 1991)

$$\underline{F}_D^{(i)}(t) = \underline{\underline{\zeta}}^{(i)} \cdot (\underline{U}^{(i)} - \underline{v}), \tag{13}$$

where the superscript (i) denotes an individual particle in the ensemble, $\underline{U}^{(i)}$ is the velocity of the particle, and $\underline{v}$ is the unperturbed velocity of the fluid evaluated at the particle position, and $\underline{\underline{\zeta}}^{(i)}$ is the resistance matrix. For prolate spheroids the resistance matrix $\underline{\underline{\zeta}}^{(i)}$ is described in terms of the orientation vector $\underline{p}^{(i)}$ by the relations

$$\underline{\underline{\zeta}}^{(i)} = \eta\{(X_A^{(i)} - Y_A^{(i)})\underline{p}^{(i)}\underline{p}^{(i)} + Y_A^{(i)}\underline{\underline{I}}\}, \tag{14}$$

$$\frac{X_A}{6\pi a} = \frac{8}{3} \cdot \frac{s^3}{-2s + (1+s^2)\mathrm{Z}}, \tag{15}$$

$$\frac{Y_A}{6\pi a} = \frac{16}{3} \cdot \frac{s^3}{2s + (3s^2-1)\mathrm{Z}}, \tag{16}$$

$$\mathrm{Z} = \ln\frac{(1+s)}{(1-s)}. \tag{17}$$

In a similar manner, the drag–torque in the angular momentum balance is given by (Satoh, 2003; Kim and Karrila, 1991)

$$\underline{\mathrm{T}}_D^{(i)}(t) = \underline{\underline{\xi}}^{(i)} \cdot (\Omega^{(i)} - \omega) + \underline{\underline{\chi}}^{(i)} : \underline{\underline{D}} \tag{18}$$

in which $\underline{\underline{D}}$ and $\underline{\omega}$ are the fluid stretching tensor and angular velocity vector (i.e., one half the vorticity), respectively, given by

$$\underline{\underline{D}} = \tfrac{1}{2}(\nabla\underline{v} + \nabla\underline{v}^{\mathrm{T}}), \tag{19}$$

$$\underline{\omega} = \tfrac{1}{2}\nabla \times \underline{v} \tag{20}$$

and the resistance matrices $\underline{\underline{\xi}}^{(i)}$ and $\underline{\underline{\chi}}^{(i)}$ are defined by the relations

$$\underline{\underline{\xi}}^{(i)} = \eta\{(X_C^{(i)} - Y_C^{(i)})\underline{p}^{(i)}\underline{p}^{(i)} + Y_C^{(i)}\underline{\underline{I}}\}, \tag{21}$$

$$\underline{\underline{\chi}}^{(i)} = \eta Y_H^{(i)}(\underline{\underline{\varepsilon}} \cdot \underline{p}^{(i)}\underline{p}^{(i)}), \tag{22}$$

$$\frac{X_C}{8\pi a^3} = \frac{4}{3} \cdot \frac{s^3(1-s^2)}{2s - (1-s^2)\mathrm{Z}}, \tag{23}$$

$$\frac{Y_C}{8\pi a^3} = \frac{4}{3} \cdot \frac{s^3(2-s^2)}{-2s + (1+s^2)\mathrm{Z}}, \tag{24}$$

$$\frac{Y_H}{8\pi a^3} = \frac{4}{3} \cdot \frac{s^5}{-2s + (1+s^2)\mathrm{Z}}, \tag{25}$$

where $\underline{\underline{\varepsilon}}$ is third-order Levi-Civita tensor.

Under the assumptions of negligible translational and rotational inertia, i.e., $m\mathrm{d}\underline{U}/\mathrm{d}t \approx 0$ and $\underline{\underline{M}}\mathrm{d}\underline{\Omega}/\mathrm{d}t \approx 0$, the governing equations for an ensemble of ellipsoids, individually denoted by the superscript (i), can be written as

$$\frac{\mathrm{d}\underline{R}^{(i)}}{\mathrm{d}t} = \underline{v}(\underline{R}^{(i)}) + [\underline{\underline{\zeta}}^{(i)}]^{-1} \cdot \left(\underline{F}_B^{(i)}(t) + \sum_j \underline{F}_j^{(i)}\right), \tag{26}$$

$$\underline{\Omega}^{(i)} = \underline{\omega}(\underline{R}^{(i)}) - [\underline{\underline{\xi}}^{(i)}]^{-1} \cdot \underline{\underline{\chi}}^{(i)} : \underline{\underline{D}} + [\underline{\underline{\xi}}^{(i)}]^{-1} \cdot \left(\underline{\mathrm{T}}_B^{(i)}(t) + \sum_j \underline{\mathrm{T}}_j^{(i)}\right). \tag{27}$$

The resistance matrices have the analytical inverses

$$[\underline{\underline{\zeta}}^{(i)}]^{-1} = \frac{1}{\eta}\left\{\left(\frac{1}{X_A^{(i)}} - \frac{1}{Y_A^{(i)}}\right)\underline{p}^{(i)}\underline{p}^{(i)} + \frac{1}{Y_A^{(i)}}\underline{\underline{I}}\right\}, \tag{28}$$

$$[\underline{\underline{\xi}}^{(i)}]^{-1} = \frac{1}{\eta}\left\{\left(\frac{1}{X_C^{(i)}} - \frac{1}{Y_C^{(i)}}\right)\underline{p}^{(i)}\underline{p}^{(i)} + \frac{1}{Y_C^{(i)}}\underline{\underline{I}}\right\}. \tag{29}$$

It is more convenient to work with the Jeffery form of Eq. (27). Taking the cross product of both sides yields

$$\underline{p}^{(i)} \times \underline{\Omega}^{(i)} = \underline{p}^{(i)} \times \underline{\omega} - \underline{p}^{(i)} \times [\underline{\underline{\xi}}^{(i)}]^{-1} \cdot \underline{\underline{\chi}}^{(i)} : \underline{\underline{D}} + \underline{p}^{(i)} \times [\underline{\underline{\xi}}^{(i)}]^{-1} \cdot \underline{\mathrm{T}}_B^{(i)}(t) \tag{30}$$

which can be converted to the form (see Appendix B)

$$\frac{\mathrm{d}}{\mathrm{d}t}(\underline{p}^{(i)}) = -\underline{\underline{W}} \cdot \underline{p}^{(i)} + \lambda_p(\underline{\underline{D}} \cdot \underline{p}^{(i)} - \underline{\underline{D}} : \underline{p}^{(i)}\underline{p}^{(i)}\underline{p}^{(i)}) + \underline{p}^{(i)} \times [\underline{\underline{\xi}}^{(i)}]^{-1} \cdot \left(\underline{\mathrm{T}}_B^{(i)}(t) + \sum_j \underline{\mathrm{T}}_j^{(i)}\right), \tag{31}$$

where $\underline{\underline{W}}$ is the vorticity tensor given by

$$\underline{\underline{W}} = \tfrac{1}{2}(\nabla \underline{v} - \nabla \underline{v}^{\mathrm{T}}) \tag{32}$$

and the quantity λ_p is a function of the particle aspect ratio, $\mathfrak{R} = a/b$, according to

$$\lambda_p = \frac{\mathfrak{R}^2 - 1}{\mathfrak{R}^2 - 1}. \tag{33}$$

Eqs. (26) and (31) constitute the governing equations for the model. These equations for the particle motions can be described as a stochastic form of the linear momentum balance with orientation dependent drag and diffusion coefficients, and a stochastic form of the Jeffery equation with orientation dependent rotational diffusion (Satoh, 2003; Kim and Karrila, 1991). In order for the dynamics to satisfy the fluctuation–dissipation theorem, the values for the Brownian forces and torques must satisfy the relationships (Cobb and Byron, 2005; Cobb and Butler, 2006)

$$\langle \underline{F}_B^{(i)}(t) \rangle = 0, \tag{34}$$

$$\langle \underline{\mathrm{T}}_B^{(i)}(t) \rangle = 0, \tag{35}$$

$$\langle \underline{F}_B^{(i)}(t) \underline{F}_B^{(i)}(t') \rangle = 2kT \underline{\underline{\zeta}}^{(i)} \delta(t - t'), \tag{36}$$

$$\langle \underline{\mathrm{T}}_B^{(i)}(t) \underline{\mathrm{T}}_B^{(i)}(t') \rangle = 2kT \underline{\underline{\xi}}^{(i)} \delta(t - t'), \tag{37}$$

where k is Boltzmann's consant, T is the absolute temperature, δ_{ij} is the Kronecker delta, $\delta(t-t')$ is the direct delta function, and the operator $\langle \ldots \rangle$ indicates an average over the ensemble of the random force. The Brownian force term can be decomposed as (Satoh, 2003)

$$[\underline{\underline{\zeta}}^{(i)}]^{-1} \cdot \underline{F}_B^{(i)} = \frac{F_{B,\parallel}^{(i)}}{\zeta_\parallel^{(i)}} \underline{p}^{(i)} + \frac{F_{B,\perp 1}^{(i)}}{\zeta_{\perp 1}^{(i)}} \underline{p}_{\perp 1}^{(i)} + \frac{F_{B,\perp 2}^{(i)}}{\zeta_{\perp 2}^{(i)}} \underline{p}_{\perp 2}^{(i)}, \tag{38}$$

where the forces $F_{B,\parallel}^{(i)}$, $F_{B,\perp 1}^{(i)}$ and $F_{B,\perp 2}^{(i)}$ are the Brownian forces and drag coefficients parallel and perpendicular to the orientation of the ellipsoids with magnitude

$$F_{B,\parallel}^{(i)} = \zeta_\parallel^{(i)} \sqrt{\frac{2 \cdot d \cdot D_{T,\parallel}^{(i)}}{\Delta t}} \cdot r_\parallel^{(i)}, \tag{39}$$

$$F_{B,\perp 1}^{(i)} = \zeta_{\perp 1}^{(i)} \sqrt{\frac{2 \cdot d \cdot D_{T,\perp 1}^{(i)}}{\Delta t}} \cdot r_{\perp 1}^{(i)}, \tag{40}$$

$$F_{B,\perp 2}^{(i)} = \zeta_{\perp 2}^{(i)} \sqrt{\frac{2 \cdot d \cdot D_{T,\perp 2}^{(i)}}{\Delta t}} \cdot r_{\perp 2}^{(i)}, \tag{41}$$

where $r_\parallel^{(i)}, r_{\perp 1}^{(i)}$ and $r_{\perp 2}^{(i)}$ are a normalized set of random numbers, the scalar d is the dimension of the system, and the translational drag and diffusion coefficients are given respectively by the relations

$$\zeta_\parallel^{(i)} = \eta X_A^{(i)}, \tag{42}$$

$$\zeta_{\perp 1}^{(i)} = \zeta_{\perp 2}^{(i)} = \zeta_\perp^{(i)} = \eta Y_A^{(i)}, \tag{43}$$

$$D_{T,\parallel}^{(i)} = \frac{kT}{\zeta_\parallel^{(i)}}, \tag{44}$$

$$D_{T,\perp 1}^{(i)} = D_{T,\perp 2}^{(i)} = \frac{kT}{\zeta_\perp^{(i)}}. \tag{45}$$

The orientation vectors $\underline{p}_{\perp 1}^{(i)}$ and $\underline{p}_{\perp 2}^{(i)}$ are given in Appendix A.

In a similar manner, the Brownian term for the torque can be decomposed as

$$[\underline{\underline{\xi}}^{(i)}]^{-1} \cdot \mathrm{T}_B^{(i)}(t) = \frac{\mathrm{T}_{B,\parallel}^{(i)}}{\xi_\parallel^{(i)}} \underline{p}^{(i)} + \frac{\mathrm{T}_{B,\perp 1}^{(i)}}{\xi_{\perp 1}^{(i)}} \underline{p}_{\perp 1}^{(i)} + \frac{\mathrm{T}_{B,\perp 2}^{(i)}}{\xi_{\perp 2}^{(i)}} \underline{p}_{\perp 2}^{(i)}, \tag{46}$$

where the torques $\mathrm{T}_{B,\parallel}^{(i)}$, $\mathrm{T}_{B,\perp 1}^{(i)}$ and $\mathrm{T}_{B,\perp 2}^{(i)}$ are the Brownian torques parallel and perpendicular to the orientation of the ellipsoids with magnitude

$$\mathrm{T}_{B,\parallel}^{(i)} = \xi_\parallel^{(i)} \sqrt{\frac{2 \cdot d \cdot D_{R,\parallel}^{(i)}}{\Delta t}} \cdot r_\parallel^{(i)}, \tag{47}$$

$$\mathrm{T}_{B,\perp 1}^{(i)} = \xi_{\perp 1}^{(i)} \sqrt{\frac{2 \cdot d \cdot D_{R,\perp 1}^{(i)}}{\Delta t}} \cdot r_{\perp 1}^{(i)}, \tag{48}$$

$$\mathrm{T}_{B,\perp 2}^{(i)} = \xi_{\perp 2}^{(i)} \sqrt{\frac{2 \cdot d \cdot D_{R,\perp 2}^{(i)}}{\Delta t}} \cdot r_{\perp 2}^{(i)}, \tag{49}$$

where $r_\parallel^{(i)}$, $r_{\perp 1}^{(i)}$ and $r_{\perp 2}^{(i)}$ are a second normalized set of random numbers, and the rotational drag and diffusion coefficients are given by

$$\xi_\parallel^{(i)} = \eta X_C^{(i)}, \tag{50}$$

$$\xi_{\perp 1}^{(i)} = \xi_{\perp 2}^{(i)} = \xi_\perp^{(i)} = \eta Y_C^{(i)}, \tag{51}$$

$$D_{R,\parallel}^{(i)} = \frac{kT}{\xi_\parallel^{(i)}}, \tag{52}$$

$$D_{R,\perp 1}^{(i)} = D_{R,\perp 2}^{(i)} = \frac{kT}{\xi_\perp^{(i)}}. \tag{53}$$

Using these relations and neglecting other forces, the model equations are given as (see Appendix C)

$$\frac{\mathrm{d}\underline{R}^{(i)}}{\mathrm{d}t} = \underline{v}(\underline{R}^{(i)}) + \frac{F_{B,\parallel}^{(i)}}{\zeta_\parallel^{(i)}} \underline{p}^{(i)} + \frac{F_{B,\perp 1}^{(i)}}{\zeta_{\perp 1}^{(i)}} \underline{p}_{\perp 1}^{(i)} + \frac{F_{B,\perp 2}^{(i)}}{\zeta_{\perp 2}^{(i)}} \underline{p}_{\perp 2}^{(i)}, \tag{54}$$

$$\frac{\mathrm{d}}{\mathrm{d}t}(\underline{p}^{(i)}) = -\underline{\underline{W}} \cdot \underline{p}^{(i)} + \lambda(\underline{\underline{D}} \cdot \underline{p}^{(i)} - \underline{\underline{D}} : \underline{p}^{(i)} \underline{p}^{(i)} \underline{p}^{(i)}) + \left(\frac{\mathrm{T}_{B,\perp 2}^{(i)}}{\xi_{\perp 2}^{(i)}} \underline{p}_{\perp 1}^{(i)} - \frac{\mathrm{T}_{B,\perp 1}^{(i)}}{\xi_{\perp 1}^{(i)}} \underline{p}_{\perp 2}^{(i)} \right). \tag{55}$$

2.3. Model equation for FFF

In flow-FFF, the velocity profile in the throughput direction is parabolic, and the cross-flow velocity is uniform. Thus, the fluid velocity vector has two non-zero components, $\underline{v} = [v_x, v_y, 0]$. The x-velocity is given by

$$v_x = \frac{h^2}{2\eta}\left(-\frac{\partial P}{\partial x}\right)\left[1 - \frac{y^2}{h^2}\right], \tag{56}$$

where h is the half gap width, and the pressure drop is express in terms of the throughput flowrate as $(-\partial P/\partial x) = 12\mu Q_x/WH^3$, where W is the thickness in the third direction. The y-velocity is specified as $v_y = Q_y/LW$, where Q_y is the cross-flow flowrate. Under these conditions, the governing equations for the fiber motion are given by (see Appendix D)

$$\frac{\mathrm{d}R_x^{(i)}}{\mathrm{d}t} = v_x + \left(\frac{F_{B,\parallel}^{(i)}}{\zeta_\parallel^{(i)}} p_x^{(i)} + \frac{F_{B,\perp 1}^{(i)}}{\zeta_{\perp 1}^{(i)}} p_{\perp 1,x}^{(i)} + \frac{F_{B,\perp 2}^{(i)}}{\zeta_{\perp 2}^{(i)}} p_{\perp 2,x}^{(i)}\right), \tag{57}$$

$$\frac{\mathrm{d}R_y^{(i)}}{\mathrm{d}t} = v_y + \left(\frac{F_{B,\parallel}^{(i)}}{\zeta_\parallel^{(i)}} p_y^{(i)} + \frac{F_{B,\perp 1}^{(i)}}{\zeta_{\perp 1}^{(i)}} p_{\perp 1,y}^{(i)} + \frac{F_{B,\perp 2}^{(i)}}{\zeta_{\perp 2}^{(i)}} p_{\perp 2,y}^{(i)}\right), \tag{58}$$

$$\frac{\mathrm{d}R_z^{(i)}}{\mathrm{d}t} = v_z + \left(\frac{F_{B,\parallel}^{(i)}}{\zeta_\parallel^{(i)}} p_z^{(i)} + \frac{F_{B,\perp 1}^{(i)}}{\zeta_{\perp 1}^{(i)}} p_{\perp 1,z}^{(i)} + \frac{F_{B,\perp 2}^{(i)}}{\zeta_{\perp 2}^{(i)}} p_{\perp 2,z}^{(i)}\right), \tag{59}$$

$$\frac{\mathrm{d}}{\mathrm{d}t}(p_x^{(i)}) = \frac{1}{2}\frac{\partial v_x}{\partial y} p_y^{(i)}[1 + \lambda(1 - 2p_x^{(i)} p_x^{(i)})] + \left(\frac{\mathrm{T}_{B,\perp 2}^{(i)}}{\xi_{\perp 2}^{(i)}} p_{\perp 1,x}^{(i)} - \frac{\mathrm{T}_{B,\perp 1}^{(i)}}{\xi_{\perp 1}^{(i)}} p_{\perp 2,x}^{(i)}\right), \tag{60}$$

$$\frac{\mathrm{d}}{\mathrm{d}t}(p_y^{(i)}) = \frac{1}{2}\frac{\partial v_x}{\partial y} p_x^{(i)}[-1 + \lambda(1 - 2p_y^{(i)} p_y^{(i)})] + \left(\frac{\mathrm{T}_{B,\perp 2}^{(i)}}{\xi_{\perp 2}^{(i)}} p_{\perp 1,y}^{(i)} - \frac{\mathrm{T}_{B,\perp 1}^{(i)}}{\xi_{\perp 1}^{(i)}} p_{\perp 2,y}^{(i)}\right), \tag{61}$$

$$\frac{\mathrm{d}}{\mathrm{d}t}(p_z^{(i)}) = -\lambda p_x^{(i)} p_y^{(i)} p_z^{(i)} \frac{\partial v_x}{\partial y} + \left(\frac{\mathrm{T}_{B,\perp 2}^{(i)}}{\xi_{\perp 2}^{(i)}} p_{\perp 1,z}^{(i)} - \frac{\mathrm{T}_{B,\perp 1}^{(i)}}{\xi_{\perp 1}^{(i)}} p_{\perp 2,z}^{(i)}\right), \tag{62}$$

where the velocity gradient is given by

$$\frac{\partial v_x}{\partial y} = -\frac{y}{\eta}\left(-\frac{\partial P}{\partial x}\right). \tag{63}$$

Eqs. (57)–(62) constitute the model equations used to solve for the particle dynamics in flow-FFF. These are integrated forward in time for each particle in the ensemble based on initial conditions for particle position and orientation using a first-order Euler integration scheme. The code is written in MATLAB.[3] An important part of the scheme is the interaction of the particles with the boundaries. The cross-flow velocity continually drives the particles towards the accumulation wall and the diffusion step being random may also cause the particles to overstep this boundary. To handle this, after each time step, it is determined whether or not any particles have advected/diffused across the lower surface and their positions are reset to the point at which they collided with the wall. At subsequent time steps, such particles are then allowed to undergo positive diffusion away from the surface. Since the length scale in the third direction in flow-FFF is generally around 100 times larger than the field direction and there is no flow component in this direction, interaction of particles with these walls is ignored.

3. Results

3.1. Diffusion

In order to test the algorithm, simulations were carried out for ellipsoidal particles in the absence of flow to ensure that the Brownian motion of the particles is being computed in the correct manner. Two cases were considered. In the first case, the particles were allowed to freely translate and rotate, and in the second case they were allowed to translate while being held at fixed orientation.

For the case of both free translation and rotation, although the particles are anisotropic, in the absence of flow they experience all orientations equally due to rotational diffusion, and thus, the effective translational diffusion coefficient is isotropic. An approximate analytical solution for the effective translational diffusion coefficient for this case was derived by Perrin (1936), and is given by

$$D = \frac{\left(\frac{kT}{6\pi\eta a}\right)}{\sqrt{1 - \left(\frac{b}{a}\right)^2}} \ln\left[\frac{1 + \sqrt{1 - \left(\frac{b}{a}\right)^2}}{\left(\frac{b}{a}\right)}\right]. \tag{64}$$

Comparison of simulation values with Eq. (64) for a range of particle sizes are shown in Table 2 for $N = 1000$ particles, and good agreement between theory and simulation is achieved. Values for the two cases fall within 3–10% of each other.

Translational diffusion with uniformly fixed particle orientations was also examined for a complete range of orientations. This was done by computing the effective diffusion coefficients along the coordinate axes, and comparing these values with the analytical values obtained from the prolate spheroid model. The analytical values along the axes were obtained by using the principal values given by Eqs. (44)–(45) and applying the similarity transform at the appropriate angle. Results comparing

[3] Identification of a commercial product is made only to facilitate reproducibility and to adequately describe procedure. In no case does it imply endorsement by the National Institute of Standards and Technology (NIST) or imply that it is necessarily the best product for the procedure.

Table 2
Comparison of effective diffusion coefficients computed by the simulation with the approximate analytical solution of Perrin (1936) for an ensemble of $N = 1000$ particles

a (m)	b (m)	$\Re$	D_{eff} (m^2/s), Perrin	D_{eff} (m^2/s), Simulation	% Difference
2×10^{-7}	1×10^{-7}	2	1.63×10^{-12}	1.69×10^{-12}	3.77
2×10^{-6}	1×10^{-7}	20	3.96×10^{-13}	4.28×10^{-13}	7.95
2×10^{-5}	1×10^{-7}	200	6.43×10^{-14}	7.06×10^{-14}	9.85

Table 3
Comparison between the model and simulation values for the diffusion coefficients along the coordinate axes for the diffusion of prolate ellipsoids at a fixed orientation of 45° for an ensemble of $N = 1000$ particles

a (m)	b (m)	D_{xx} (m^2/s), Model	D_{yy} (m^2/s), Model	D_{xx} (m^2/s), Simulation	D_{yy} (m^2/s), Simulation	Max Difference
2×10^{-5}	1×10^{-7}	7.03×10^{-14}	7.03×10^{-14}	7.02×10^{-14}	6.99×10^{-14}	5%

simulation results with the analytical values for particles diffusing at a fixed angle of 45° are shown in Table 3, for $N = 1000$ particles. It can be seen that the particles diffuse in the correct anisotropic manner with the correct magnitude along the coordinate axes. Together, the two diffusion cases examined indicate that the Brownian motion of the particles is being computed in the correct manner.

3.2. Solution of Jeffery's equation

The integration algorithm for Jeffery's equation was also tested. For an ellipsoid in 2D, steady shear flow in the absence of Brownian motion, there is an analytical solution describing the orientation, ϕ, and period, T, for the in-plane rotation of the particles (Jeffery, 1922). These are given by the relations

$$\tan\phi = \Re \tan\left(\frac{2\pi t}{T}\right), \tag{65}$$

$$T = \frac{2\pi}{\dot{\gamma}}\left(\Re + \frac{1}{\Re}\right). \tag{66}$$

For Brownian systems, the behavior is a function of a rotational Peclet number which we define as

$$Pe = \frac{\dot{\gamma}}{(kT/\eta Y_c)}. \tag{67}$$

The behavior described by Eqs. (65)–(66) corresponds to the case of no rotational diffusion, or infinite Peclet number. Thus, the behavior of the system can be expected to increasingly diverge from this result as the Peclet number gets smaller.

Simulations of Jeffery's equation for the non-Brownian case were compared with the analytical solution for a variety of parameter conditions. A solution for the components of the orientation vector for a particle size of $L_p = 10\,\mu m$, $\Re = 10$ at a shear rate of $\dot{\gamma} = 100\,s^{-1}$ under non-Brownian conditions are shown in Fig. 6a and are plotted as a function of $\tau = t/T$. It can be seen that at this aspect ratio, the particles spend most of their time oriented in the flow direction, and then quickly flip every half period. There is no out of plane rotation (as seen by the constant null value of p_z). The value of the period calculated from the simulation compares to four significant figures with the analytical value of $T = 0.634602\,s$. In general, integration of the non-Brownian system was straightforward and found to be virtually indistinguishable from the analytical solution at all particle aspect ratios above 10, with little sensitivity the time step used in the simulation.

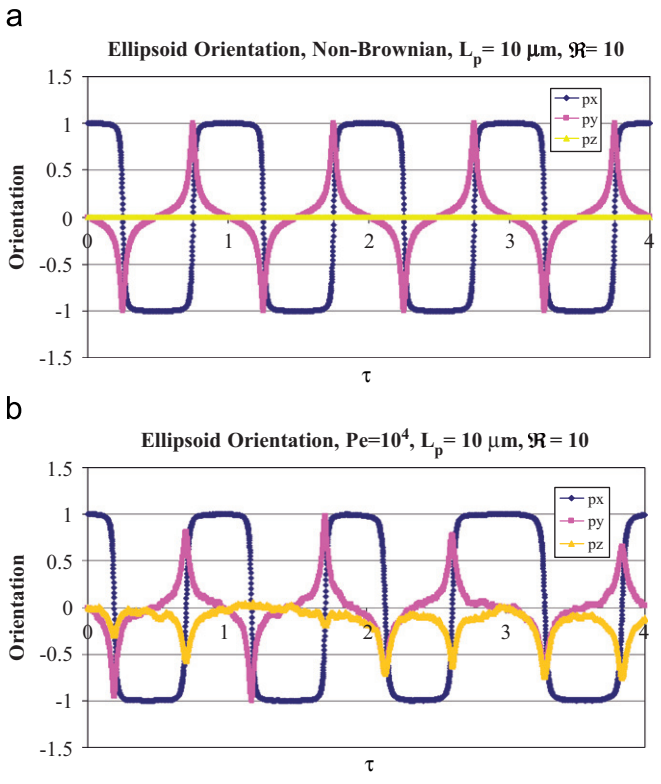

Fig. 6. Simulation of Jeffery's equation for the orientation of 10 μm particles with $\Re = 10$ and $\dot{\gamma} = 100\,s^{-1}$. (a) Non-Brownian case which is in tacit agreement with the analytical solution. (b) Brownian flow for which the rotational Peclet number is approximately $Pe = 10^4$.

A solution to Jeffery's equation under stochastic conditions, for the same particle size and shear rate as the previous case is shown in Fig. 6b. Under these conditions the Peclet number is approximately $Pe = 10^4$, and diffusion has only a moderate effect. The behavior is qualitatively similar to that which is seen for the non-Brownian case with the main differences being that the period becomes slightly irregular, and the particles tend to briefly "kayak" out of plane when they flip (Tao et al., 2005a) as seen in the graph for p_z which exhibits distinct spikes in the time series as it fluctuates about the in-plane rotation value of zero. A highly stochastic system is shown the series of Figs. 7a–c, which compares the components of the Brownian orientation vector with the non-Brownian case for $L_p = 1\,\mu\text{m}$, $\Re = 10$ and $\dot{\gamma} = 100\,\text{s}^{-1}$. Under these conditions the Peclet number is reduced to approximately $Pe = 10$, and diffusion has a much more pronounced effect. In the time series for p_x, shown in Fig. 7a, there is still evidence of "flipping" between orientations. However, the frequency of the transition is increased and the orientation in the flow direction is not steady, but instead undergoes a pronounced chaotic wobble before flipping. This result, together with the time series for p_y and p_z (Figs. 7b and c), indicates that under these conditions the fibers experience what is essentially random orientation.

These results indicate that the diffusion which governs the particle retention depends on the Peclet number. At high Peclet numbers the particles spend the majority of the time oriented in the flow direction, and thus, it is appropriate to calculate the retention in terms of the transverse diffusion coefficient of the model, $D = kT/\eta Y_A$. However, at low Peclet numbers the particle orientation becomes more random and it can be expected that the Perrin diffusivity (Eq. (64)) is more appropriate for describing the retention. In terms of nanotube separations in FFF, tubes are typically micron to sub micron in length with aspect ratios much greater than those in Fig. 7. Thus, in the range of shear rates characteristic of these devices, it can be expected that the Peclet number will be quite low, and that the Perrin diffusivity is generally the appropriate quantity to use for the retention calculation.

3.3. Particle dispersion in flow-FFF

To compute solutions for the case of flow-FFF, the particles are all started from the same initial point at the channel entrance just above the lower wall to mimic the experimental practice of focusing.[4] In all cases reported here, the solutions were assumed to be aqueous at 293 K. Fig. 8a shows the position of a uniform mixture of 1 nm diameter ellipsoids with an aspect ratio of $\Re = 100$ for $N = 1000$ particles shortly after startup, for the parameters shown in Table 4. A detail of the particle cloud is shown in Fig. 8b. The dispersion of the particles along the throughput axis is evident. The dispersion occurs due to the interaction between the parabolic velocity profile and the random Brownian motion in the cross flow direction. Particles that experience more upward diffusion are swept further along downstream than particles that diffused closer to the surface.

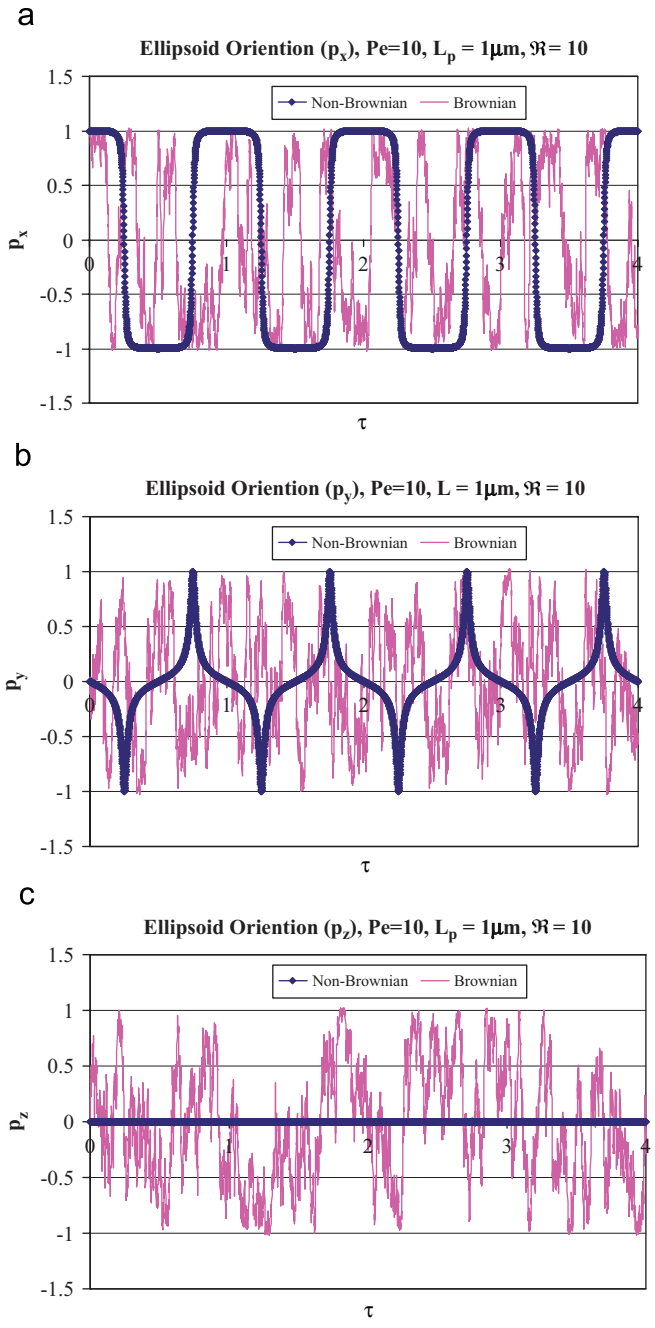

Fig. 7. Comparison of non-Brownian and Brownian simulations of Jeffery's equation for the orientation of 1 μm particles with $\Re = 10$ and $\dot{\gamma} = 100\,\text{s}^{-1}$. For the Brownian case, the rotational Peclet number is approximately $Pe = 10$. (a) p_x. (b) p_y. (c) p_z.

The behavior of the particle cloud is shown in Figs. 9a and b. Fig. 9a shows the maximum, average, and minimum particle positions in the axial direction vs. time, while Fig. 9b shows the average cross-sectional position vs. time. In all these curves, the slope reflects the average velocity of the particles. In the axial direction, the maximum, average and minimum particle

[4] In practice, the sample to be separated in FFF is injected into the channel and the flow is initially run in reverse so that the initially circular injection spot is compressed into a band at the entrance gate. Focusing narrows the elution peaks.

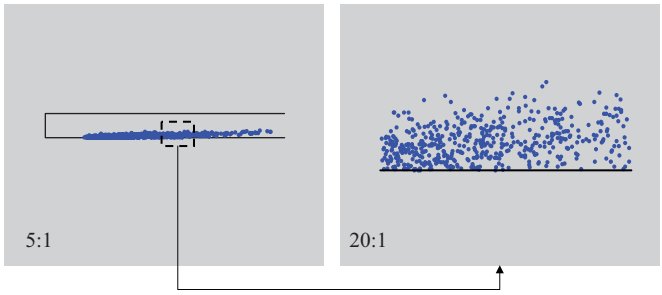

Fig. 8. Startup flow showing dispersion (spreading) of ellipsoids in flow-FFF for a monodisperse mixture with $\mathfrak{R}=100$ and $N=1000$ particles. All particles start from identical initial positions. Dispersion occurs due to the interplay between the transverse diffusion and the parabolic velocity field. (a) Wide angle view of the dispersion close to the inlet. (b) Details of the particle cloud. The scale is blown up by a factor of 20 in the y-direction.

Table 4
Parameters used for simulation in Figs. 8–10

a (m)	b (m)	L (m)	W (m)	H (mm)	Q_x (m^3/s)	Q_y (m^3/s)
0.5×10^{-7}	0.5×10^{-9}	0.2	0.01	0.1	2×10^{-9}	2×10^{-9}

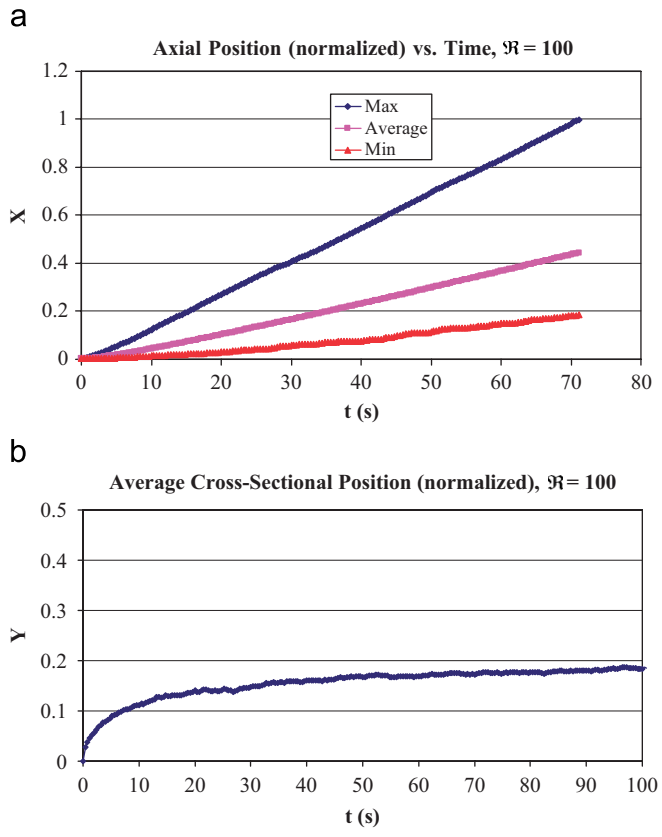

Fig. 9. The positional behavior of the particle cloud. (a) The maximum, average, and minimum particle positions in the axial direction vs. time. The ordinate is plotted in the dimensionless unit $X = x/L$. (b) Average cross-sectional position vs. time. The ordinate is plotted in the dimensionless unit $Y = y/H$.

velocities all have different slopes. Thus, the cloud continues to stretch in the axial direction as it elutes. The average y-position shown in Fig. 9b indicates that the particles quickly come to an average equilibrium position which stays relatively constant throughout the process.

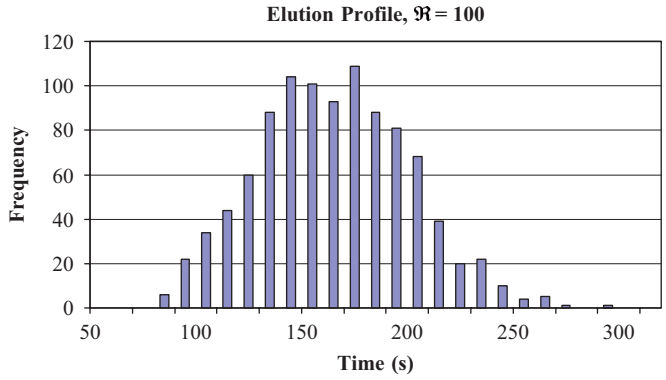

Fig. 10. Elution histogram for a flow-FFF simulation of a monodisperse mixture of ellipsoids with $\mathfrak{R}=100$ and $N=1000$ particles.

Table 5
Comparison of theoretical and simulated residence times for the simulation in Figs. 8–10, with $\mathfrak{R}=100$ and $N=1000$ particles

Theory				Simulation			
Retention	t_{min} (s)	t_0 (s)	t_r (s)	Mean (s)	Standard deviation (s)	Min (s)	Max (s)
0.778	66.7	133.3	171.4	155.2	35.8	71.2	286.6

Table 6
Parameters used for the simulations in Figs. 11–12

Case	L (m)	W (m)	H (mm)	Q_x (m^3/s)	Q_y (m^3/s)
1	0.2	0.01	0.1	2×10^{-9}	2×10^{-9}
2	0.2	0.01	0.1	2×10^{-9}	4×10^{-9}

The dispersion of the particles gives rise to an elution profile which is shown in Fig. 10. For this case, the distribution has a slightly positive skewness (0.21) about the mean. The statistics of the distribution are shown in Table 5 and compared with the values for the theoretical minimum residence and retention times. The Perrin diffusion coefficient of the ellipsoids was used to calculate the retention. The minimum simulated transit time is quite close to the theoretical minimum, but the maximum is much larger than the theoretical retention time. Thus, the simulated distribution is a bit broader than that based on theory.

3.4. Separations in flow-FFF

Simulations were carried out for a mixture of 1 nm diameter ellipsoids, for aspect ratios of $\mathfrak{R}=[10, 100, 300, 1000]$, for the conditions labeled Case 1 in Table 6. The elution profiles for the simulations are shown in full in Fig. 11a, and in detail in Fig. 11b. Minimum, mean and maximum elution times are listed in Table 7. It is evident from the figures and the data that the 1000 nm particles become completely separated from the rest of the mixture, but the elution profiles for the other

particles overlap, as shown in Fig. 11b. If analyzed as pairs, the 100 nm particles are significantly overlapped with both the 10 and 300 nm fractions. However, the 300 nm fraction is only minimally overlapped with the 10 nm in terms of the height of the frequency in the area of overlap. These results seem to point to the ratio of retentions as being a significant factor in achieving clean separations. For example, the ratio of the 300–1000 nm retention is about 2.5, and the ratio of the 10–300 nm retention values is about 2.2. These fractions contain either no, or minimal overlap. On the contrary, the 10 nm/100 nm and 100 nm/300 nm retention ratios are less than 2, and these fractions are significantly overlapped.

To further test this hypothesis, simulations were carried out for a mixture of 1 nm diameter ellipsoids, for aspect ratios of $\mathfrak{R}=[10, 100, 300]$, for the conditions labeled Case 2 in Table 6. For this run, the cross-flow flowrate has been doubled, and while this has the effect of lowering all the retention values individually, is also raises the 10 nm/100 nm and 100 nm/300 nm retention ratios to values greater than or much closer to 2. Results for this run are shown in Fig. 12. It is evident from this figure the retention ratio is a significant factor in the separations, as the 100 nm/300 nm particles are completely separated (ratio = 2.1), and the 10–100 nm particles have only a minimal overlap (ratio = 1.8) with their right and left tails respectively.

To further investigate this, the minimum particle velocity of the fast moving component is compared with the maximum particle velocity of the slow moving component for the 10 nm/100 nm and the 100 nm/300 nm fractions, for both Cases 1 and 2. These results are shown in Table 8. The results show that increasing the retention ratio between components systematically lowers difference between the minimum velocity of the fast mover and the maximum velocity of the slow mover until the one overtakes the other. This result is significant because it shows that for separation to occur, the minimum velocity of fast mover must be greater,

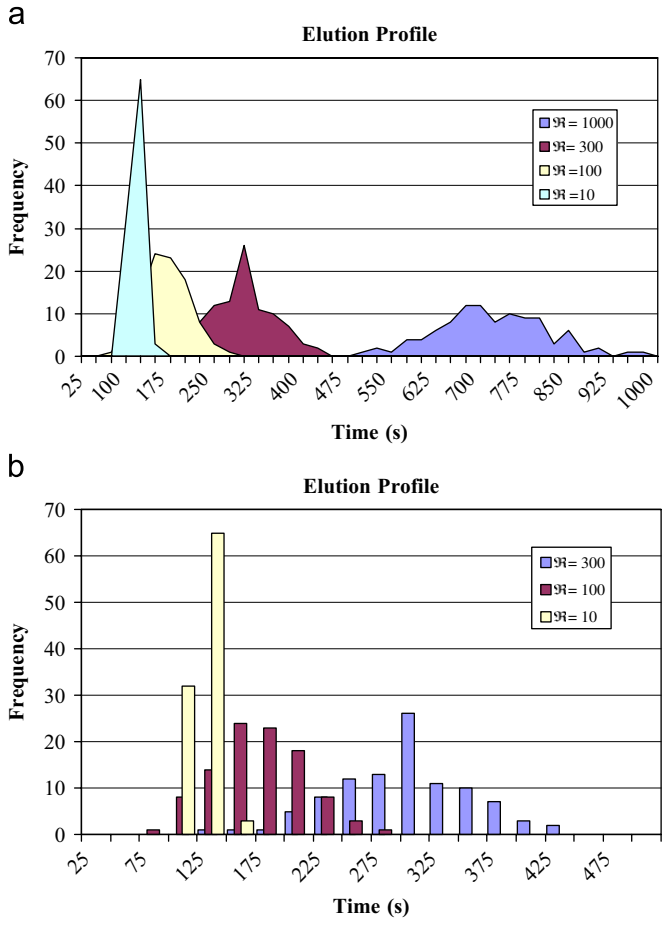

Fig. 11. (a) Elution histograms for a flow-FFF simulation of mixture of ellipsoids with $\mathfrak{R}=[10, 100, 300, 1000]$ for the processing parameters shown in Table 6, Case 1. (b) Detail of the elution histogram for $\mathfrak{R}=[10, 100, 300]$.

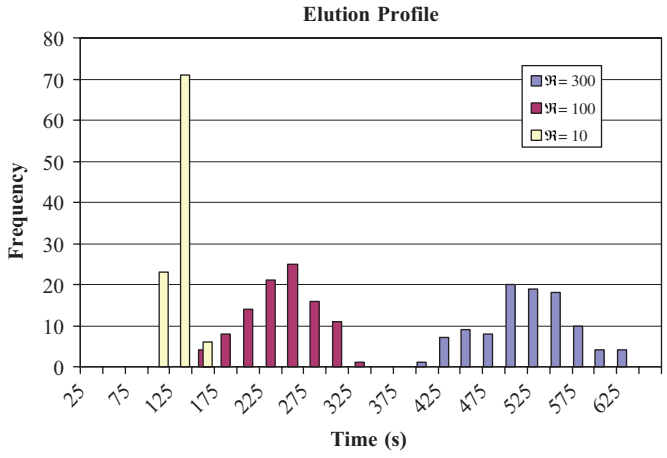

Fig. 12. Elution histograms for a flow-FFF simulation of mixture of ellipsoids with $\mathfrak{R} = [10, 100, 300]$ for the processing parameters shown in Table 6, Case 2.

Table 7
Simulated residence times for the data in Figs. 11 and 12, with $N = 100$ particles per component

Case	$\mathfrak{R}$	Retention	Minimum elution time (s)	Mean elution time (s)	Maximum elution time (s)
1	10	0.990	82.131	103.63	133.13
1	100	0.778	72.972	154.18	268.7
1	300	0.449	112.92	279.21	422.98
1	1000	0.183	475.36	706.96	973.26
2	10	0.962	84.40	108.05	137.8
2	100	0.527	125.32	224.65	308.47
2	300	0.249	392.61	503.98	624.83

Table 8
Comparison of minimum velocity of high retention component with maximum velocity of low retention component for different fractions and conditions

Fraction	Minimum velocity, high retention component (m/s)	Min vs. Max	Maximum velocity, low retention component (m/s)
10 nm/100 nm, Case 1	0.001463	$<$, no separation	0.002779
10 nm/100 nm, Case 2	0.00112	$\approx$, small overlap	0.001156
100 nm/300 nm, Case 1	0.000597	$<$, no separation	0.001687
100 nm/300 nm, Case 2	0.000613	$>$, separation	0.000503

than the maximum velocity of the slow mover and that when the proper retention ratio is achieved the particles will be separated, independent of the length of the flow channel.

4. Discussion

A Brownian dynamics simulation based on a prolate spheroid particle model has been developed to model the separation of nanotubes in flow-FFF. The simulation algorithm was tested in part by comparing results for the Brownian diffusion of prolate spheroids with the theoretical result of Perrin (1936), and excellent agreement was achieved. Simulation results also compared well with the analytical solution for Jeffery's equation in shear flow under non-Brownian conditions. In addition, the set of simulations conducted for Jeffery's equation under Brownian conditions indicated that for the range of Peclet number expected for nanotubes under typical FFF flow conditions, the retention for these particles should be described in terms of the Perrin diffusion coefficient.

Elution profiles and average velocity through the device as a function of particle size, and throughput and cross flow flowrates were examined. The simulation of flow-FFF for nanotube scale particles shows that they elute by a normal mode mechanism, based on a particle diameter of 1 nm. Comparison of the elution profiles for a mixture of particles with aspect ratios of 10–1000, showed that elution characteristics are governed by the value of the retention. Particles with retention values close to 1 elute relative quickly, with sharp peaks. As the retention ratio decreases towards zero, the total elution time increases, and the distribution becomes increasingly broad. For polydisperse mixtures, based on the results shown here, one would expect the particles to elute in fractions of every increasing size. This in fact, as has been seen in the literature (Chen and Selegue, 2002; Moon et al., 2004; Selegue et al., 2001; Tagmatarchis et al., 2005; Peng et al., 2006; Liu et al., 1998).

An important issue in FFF is obtaining clean separations of different size components. The simulation results show that the ability to achieve this is governed chiefly by the ratio of the retention values of the different components, but also partly by the absolute value of the retention. When the retention values for the different components are relatively low, the separation of fractions of different sizes can be cleanly achieved provided the ratio of their retention values is somewhat greater than 2. As the retentions become higher, retention ratios greater than 2 do not necessarily produce perfectly clean separation, but they do significantly reduce the overlap between fractions. Thus, at higher absolute retention values, greater retention ratios are needed. It is clear from these results that the best means for producing clean separations is to keep the retention value of the fastest eluting component at least twice the value of the next fastest component, while mimimizing the retention value of the second components as much as possible. For polydisperse mixtures, fractions need to be based on averages over size scales which produce significant differences in the diffusion coefficient.

The results shown here allow one to draw the conclusion that conventional flow-FFF can be expected to drive length based separation of nanotubes. However, it is also desirable to separate them according to their chirality. In future work, it is desirable to modify the simulation to investigate whether a variation of conventional flow-FFF with possibly either electric or magnetic fields can be used as a basis for separating tubes according to their electronic properties. In normal mode operation of flow-FFF, the ability to separate particles depends on the relative retention ratios of the different species, and the retention depends on the value of the parameter $\lambda = D/|v_c|H$. For particles of the comparable size but different chirality, the diffusion coefficients will be relatively similar. Thus, the only way to change the relative retention values is by changing their velocities in the cross field, i.e., $\lambda = D/Hv'$, such that the velocity v' of the metallic tubes differs from that of the semi-conductors. For example, if flow-FFF is run with an electric field acting in the opposite direction to the cross flow field, the net velocity is given by $v' = |v_c| - \mu E$ where μ is the electrophoretic mobility. Thus, the separation of componentsunder these conditions would depend on the relative mobilities of metallics and semiconductors in an electric field. Promoting such selective differences in mobility between tubes of different chirality could be a basis for creating retention differences between these different species, and thus promoting separation.

5. Summary and conclusion

A Brownian dynamics simulation based on a ellipsoidal (prolate spheroid) particle model has been developed to model the separation of nanotubes in flow-FFF. The particle motions are governed by stochastic forms of a linear momentum balance with orientation dependent drag and diffusion coefficients, and the Jeffery equation with rotational diffusion. The simulation shows that nanotube scale particles would be expected to elute by a normal mode mechanism up to aspect ratios of about 1000, based on a particle diameter of 1 nm. Separation of nanotubes

of different length is governed by the value of the retention variable for each component in agreement with theory. Elution profiles and average velocity through the device as a function of particle size, and throughput and cross flow flowrates were examined. The simulation shows that clean separations between components of different size is achieved when the ratio of the retention values is greater than 2.

Appendix A. Orientation vectors

If the orientation vector $\underline{p} = [p_x, p_y, p_z]$ is renormalized such that

$$\underline{p} = \frac{1}{\alpha}[p_x, p_y, p_z], \tag{68}$$

where $\alpha = \sqrt{p_x^2 + p_y^2 + p_z^2}$, then the components of the orientation vectors $\underline{p}_{\perp 1}$ and $\underline{p}_{\perp 2}$ are given by

$$\underline{p}_{\perp 1} = \left[\frac{-p_y}{\sqrt{p_x^2 + p_y^2}}, \frac{p_x}{\sqrt{p_x^2 + p_y^2}}, 0 \right], \tag{69}$$

$$\underline{p}_{\perp 2} = \left[\frac{-p_x p_z}{\alpha\sqrt{p_x^2 + p_y^2}}, \frac{-p_y p_z}{\alpha\sqrt{p_x^2 + p_y^2}}, \frac{p_x^2 + p_y^2}{\alpha\sqrt{p_x^2 + p_y^2}} \right]. \tag{70}$$

Appendix B. Derivation of Jeffrey's equation

The angular velocity of the particle is given by the relationship

$$\underline{\Omega}^{(i)} = \underline{\omega}(\underline{R}^{(i)}) + [\underline{\underline{\xi}}^{(i)}]^{-1} \cdot (-\underline{\underline{\chi}}^{(i)} : \underline{\underline{D}} + \underline{T}_B^{(i)}(t)). \tag{71}$$

Taking the cross product of both sides yields

$$\underline{p}^{(i)} \times \underline{\Omega}^{(i)} = \underline{p}^{(i)} \times \underline{\omega} - \underline{p}^{(i)} \times [\underline{\underline{\xi}}^{(i)}]^{-1} \cdot \underline{\underline{\chi}}^{(i)} : \underline{\underline{D}} + \underline{p}^{(i)} \times [\underline{\underline{\xi}}^{(i)}]^{-1} \cdot \underline{T}_B^{(i)}(t). \tag{72}$$

The term on the left is given by

$$\underline{p}^{(i)} \times \underline{\Omega}^{(i)} = -\frac{\mathrm{d}}{\mathrm{d}t}(\underline{p}^{(i)}). \tag{73}$$

The first term on the right simplifies as

$$\begin{aligned}
\underline{p}^{(i)} \times \underline{\omega} &= \tfrac{1}{2}\underline{p}^{(i)} \times \nabla \times \underline{v} \\
&= \tfrac{1}{2} p_n^{(i)} \nabla_j v_k [\varepsilon_{jkl}\varepsilon_{mnl}]\hat{e}_m \\
&= \tfrac{1}{2} p_n^{(i)} \nabla_j v_k [\delta_{jm}\delta_{kn} - \delta_{jn}\delta_{km}]\hat{e}_m \\
&= \tfrac{1}{2}[p_n^{(i)} \nabla_m v_n - p_n^{(i)} \nabla_n v_m]\hat{e}_m \\
&= \tfrac{1}{2}(\nabla \underline{v} \cdot \underline{p}^{(i)} - \underline{p}^{(i)} \cdot \nabla \underline{v}) \\
&= \tfrac{1}{2}(\nabla \underline{v} \cdot \underline{p}^{(i)} - \nabla \underline{v}^{\mathrm{T}} \cdot \underline{p}^{(i)}) \\
&= \tfrac{1}{2}(\nabla \underline{v} - \nabla \underline{v}^{\mathrm{T}}) \cdot \underline{p}^{(i)} \\
&= \underline{\underline{W}} \cdot \underline{p}^{(i)}
\end{aligned} \tag{74}$$

where $\underline{\underline{W}} = \frac{1}{2}(\nabla \underline{v} - \nabla \underline{v}^{\mathrm{T}})$ is the vorticity tensor.

To find the term $\underline{p}^{(i)} \times [\underline{\underline{\xi}}^{(i)}]^{-1} \cdot \underline{\underline{\chi}}^{(i)} : \underline{\underline{D}}$, first we start with the evaluation of

$$\begin{aligned}
\underline{\underline{\chi}}^{(i)} : \underline{\underline{D}} &= \eta Y_H^{(i)} (\underline{\underline{\varepsilon}} \cdot \underline{p}^{(i)} \underline{p}^{(i)}) : \underline{\underline{D}} \\
&= \eta Y_H^{(i)} (\varepsilon_{jmn} p_n^{(i)} p_k^{(i)} D_{km}) \hat{e}_j.
\end{aligned} \tag{75}$$

We then find

$$\begin{aligned}
&[\underline{\underline{\xi}}^{(i)}]^{-1} \cdot \underline{\underline{\chi}}^{(i)} : \underline{\underline{D}} \\
&= \frac{1}{\eta}\left\{ \left(\frac{1}{X_C^{(i)}} - \frac{1}{Y_C^{(i)}} \right) \underline{p}^{(i)} \underline{p}^{(i)} + \frac{1}{Y_C^{(i)}} \underline{\underline{I}} \right\} \\
&\quad \cdot \eta Y_H^{(i)} (\underline{\underline{\varepsilon}} \cdot \underline{p}^{(i)} \underline{p}^{(i)}) : \underline{\underline{D}} \\
&= \frac{Y_H^{(i)}}{Y_C^{(i)}} (\varepsilon_{jmn} p_n^{(i)} p_k^{(i)} D_{km}) \hat{e}_j
\end{aligned} \tag{76}$$

as the term $\underline{p}^{(i)} \underline{p}^{(i)} \cdot \underline{\underline{\varepsilon}} \cdot \underline{p}^{(i)} \underline{p}^{(i)} = 0$.

Finally,

$$\begin{aligned}
&\underline{p}^{(i)} \times [\underline{\underline{\xi}}^{(i)}]^{-1} \cdot \underline{\underline{\chi}}^{(i)} : \underline{\underline{D}} \\
&= p_q^{(i)} \hat{e}_q \times \frac{Y_H^{(i)}}{Y_C^{(i)}} (\varepsilon_{jmn} p_n^{(i)} p_k^{(i)} D_{km}) \hat{e}_j \\
&= p_q^{(i)} \frac{Y_H^{(i)}}{Y_C^{(i)}} (\varepsilon_{jmn} p_n^{(i)} p_k^{(i)} D_{km}) (\hat{e}_q \times \hat{e}_j) \\
&= \frac{Y_H^{(i)}}{Y_C^{(i)}} (\varepsilon_{jmn}\varepsilon_{qjr} p_q^{(i)} p_n^{(i)} p_k^{(i)} D_{km}) \hat{e}_r \\
&= \frac{Y_H^{(i)}}{Y_C^{(i)}} (\varepsilon_{mnj}\varepsilon_{rqj} p_q^{(i)} p_n^{(i)} p_k^{(i)} D_{km}) \hat{e}_r \\
&= \frac{Y_H^{(i)}}{Y_C^{(i)}} (\delta_{mr}\delta_{nq} - \delta_{mq}\delta_{nr})(p_q^{(i)} p_n^{(i)} p_k^{(i)} D_{km}) \hat{e}_r \\
&= \frac{Y_H^{(i)}}{Y_C^{(i)}} (p_q^{(i)} p_q^{(i)} p_k^{(i)} D_{kr} - p_m^{(i)} p_r^{(i)} p_k^{(i)} D_{km}) \hat{e}_r \\
&= \frac{Y_H^{(i)}}{Y_C^{(i)}} (D_{kr} p_k^{(i)} - D_{km} p_m^{(i)} p_r^{(i)} p_k^{(i)}) \hat{e}_r
\end{aligned}$$

$$= \frac{Y_H^{(i)}}{Y_C^{(i)}}(D_{rk}p_k^{(i)} - D_{km}p_m^{(i)}p_k^{(i)}p_r^{(i)})\hat{e}_r$$

$$= \frac{Y_H^{(i)}}{Y_C^{(i)}}(\underline{\underline{D}}\cdot\underline{p}^{(i)} - \underline{\underline{D}}:\underline{p}^{(i)}\underline{p}^{(i)}\underline{p}^{(i)}). \quad (77)$$

The term $Y_H^{(i)}/Y_C^{(i)} = (a^2-b^2)/(a^2+b^2) = (\Re^2-1)/(\Re^2-1)$ where $\Re = a/b$. Thus, Eq. (72) can be written as

$$\frac{\mathrm{d}}{\mathrm{d}t}(\underline{p}^{(i)}) = -\underline{\underline{W}}\cdot\underline{p}^{(i)} + \frac{\Re^2-1}{\Re^2-1}(\underline{\underline{D}}\cdot\underline{p}^{(i)} - \underline{\underline{D}}:\underline{p}^{(i)}\underline{p}^{(i)}\underline{p}^{(i)}) - \underline{p}^{(i)}\times[\underline{\underline{\xi}}^{(i)}]^{-1}\cdot\underline{\mathrm{T}}_B^{(i)}(t). \quad (78)$$

Appendix C. Evaluation of random torque term

To evaluate term $\underline{p}^{(i)}\times[\underline{\underline{\xi}}^{(i)}]^{-1}\cdot\underline{\mathrm{T}}_B^{(i)}(t)$, we note that the Brownian term for the torque can be decomposed as

$$[\underline{\underline{\xi}}^{(i)}]^{-1}\cdot\underline{\mathrm{T}}_B^{(i)}(t) = \frac{\mathrm{T}_{B,\parallel}^{(i)}}{\xi_\parallel^{(i)}}\underline{p}^{(i)} + \frac{\mathrm{T}_{B,\perp1}^{(i)}}{\xi_{\perp1}^{(i)}}\underline{p}_{\perp1}^{(i)} + \frac{\mathrm{T}_{B,\perp2}^{(i)}}{\xi_{\perp2}^{(i)}}\underline{p}_{\perp2}^{(i)}. \quad (79)$$

Thus,

$$\underline{p}^{(i)}\times[\underline{\underline{\xi}}^{(i)}]^{-1}\cdot\underline{\mathrm{T}}_B^{(i)}(t) = \underline{p}^{(i)}\times\left(\frac{\mathrm{T}_{B,\parallel}^{(i)}}{\xi_\parallel^{(i)}}\underline{p}^{(i)} + \frac{\mathrm{T}_{B,\perp1}^{(i)}}{\xi_{\perp1}^{(i)}}\underline{p}_{\perp1}^{(i)} + \frac{\mathrm{T}_{B,\perp2}^{(i)}}{\xi_{\perp2}^{(i)}}\underline{p}_{\perp2}^{(i)}\right) = \frac{\mathrm{T}_{B,\perp1}^{(i)}}{\xi_{\perp1}^{(i)}}\underline{p}_{\perp2}^{(i)} - \frac{\mathrm{T}_{B,\perp2}^{(i)}}{\xi_{\perp2}^{(i)}}\underline{p}_{\perp1}^{(i)}. \quad (80)$$

Alternatively, the torque $\underline{\mathrm{T}}_B^{(i)}$ can be expressed as a cross-product of the orientation vector with a random force $\underline{\Phi}_B^{(i)}$

$$\underline{\mathrm{T}}_B^{(i)} = \underline{p}^{(i)}\times\underline{\Phi}_B^{(i)}. \quad (81)$$

Thus,

$$\underline{p}^{(i)}\times[\underline{\underline{\xi}}^{(i)}]^{-1}\cdot\underline{\mathrm{T}}_B^{(i)} = \underline{p}^{(i)}\times[\underline{\underline{\xi}}^{(i)}]^{-1}\cdot\underline{p}^{(i)}\times\underline{\Phi}_B^{(i)}. \quad (82)$$

This can be simplified by noting

$$\underline{p}^{(i)}\times[\underline{\underline{\xi}}^{(i)}]^{-1} = \underline{p}^{(i)}\times\frac{1}{\eta}\left\{\left(\frac{1}{X_C^{(i)}} - \frac{1}{Y_C^{(i)}}\right)\underline{p}^{(i)}\underline{p}^{(i)} + \frac{1}{Y_C^{(i)}}\underline{\underline{I}}\right\} = \frac{1}{\eta Y_C^{(i)}}\underline{p}^{(i)}\times\underline{\underline{I}}. \quad (83)$$

Using this, Eq. (82) can be evaluated as

$$\begin{aligned}
&\underline{p}^{(i)}\times[\underline{\underline{\xi}}^{(i)}]^{-1}\cdot\underline{\mathrm{T}}_B^{(i)} \\
&= \left(\frac{1}{\eta Y_C^{(i)}}\underline{p}^{(i)}\times\underline{\underline{I}}\right)\cdot(\underline{p}^{(i)}\times\underline{\Phi}_B^{(i)}) \\
&= \left(\frac{1}{\eta Y_C^{(i)}}p_j^{(i)}\hat{e}_j\times\delta_{kl}\hat{e}_k\hat{e}_l\right)\cdot(p_r^{(i)}\hat{e}_r\times\Phi_{B,s}^{(i)}\hat{e}_s) \\
&= \left(\frac{1}{\eta Y_C^{(i)}}p_j^{(i)}\delta_{kl}\varepsilon_{jkm}\hat{e}_m\hat{e}_l\right)\cdot(p_r^{(i)}\Phi_{B,s}^{(i)}\varepsilon_{rst}\hat{e}_t) \\
&= \left(\frac{1}{\eta Y_C^{(i)}}p_j^{(i)}\varepsilon_{jkm}\hat{e}_m\hat{e}_k\right)\cdot(p_r^{(i)}\Phi_{B,s}^{(i)}\varepsilon_{rst}\hat{e}_t) \\
&= \frac{1}{\eta Y_C^{(i)}}p_j^{(i)}p_r^{(i)}\Phi_{B,s}^{(i)}\varepsilon_{jkm}\varepsilon_{rst}\delta_{kt}\hat{e}_m \\
&= \frac{1}{\eta Y_C^{(i)}}p_j^{(i)}p_r^{(i)}\Phi_{B,s}^{(i)}\varepsilon_{jkm}\varepsilon_{rsk}\hat{e}_m \\
&= \frac{1}{\eta Y_C^{(i)}}p_j^{(i)}p_r^{(i)}\Phi_{B,s}^{(i)}\varepsilon_{mjk}\varepsilon_{rsk}\hat{e}_m \\
&= \frac{1}{\eta Y_C^{(i)}}p_j^{(i)}p_r^{(i)}\Phi_{B,s}^{(i)}(\delta_{mr}\delta_{js} - \delta_{ms}\delta_{jr})\hat{e}_m \\
&= \frac{1}{\eta Y_C^{(i)}}(p_j^{(i)}p_m^{(i)}\Phi_{B,j}^{(i)} - p_j^{(i)}p_j^{(i)}\Phi_{B,m}^{(i)})\hat{e}_m \\
&= \frac{1}{\eta Y_C^{(i)}}(p_j^{(i)}p_m^{(i)}\Phi_{B,j}^{(i)} - \Phi_{B,m}^{(i)})\hat{e}_m \\
&= -\frac{1}{\eta Y_C^{(i)}}(\underline{\underline{I}} - \underline{p}^{(i)}\underline{p}^{(i)})\cdot\underline{\Phi}_B^{(i)}. \quad (84)
\end{aligned}$$

Appendix D. Jeffery's equation for shear flow

For shear flow,

$$\nabla\underline{v} = \begin{pmatrix} \frac{\partial u}{\partial x} & \frac{\partial v}{\partial x} & \frac{\partial w}{\partial x} \\ \frac{\partial u}{\partial y} & \frac{\partial w}{\partial y} & \frac{\partial w}{\partial y} \\ \frac{\partial u}{\partial z} & \frac{\partial v}{\partial z} & \frac{\partial w}{\partial z} \end{pmatrix} = \begin{pmatrix} 0 & 0 & 0 \\ \frac{\partial u}{\partial y} & 0 & 0 \\ 0 & 0 & 0 \end{pmatrix}. \quad (85)$$

The stretching tensor is

$$\underline{\underline{D}} = \frac{1}{2}(\nabla\underline{v} + \nabla\underline{v}^{\mathrm{T}}) = \frac{1}{2}\begin{pmatrix} 0 & \frac{\partial u}{\partial y} & 0 \\ \frac{\partial u}{\partial y} & 0 & 0 \\ 0 & 0 & 0 \end{pmatrix}. \quad (86)$$

The vorticity tensor is

$$\underline{\underline{W}} = \frac{1}{2}(\nabla \underline{v} - \nabla \underline{v}^{\mathrm{T}}) = \frac{1}{2}\begin{pmatrix} 0 & -\dfrac{\partial u}{\partial y} & 0 \\ \dfrac{\partial u}{\partial y} & 0 & 0 \\ 0 & 0 & 0 \end{pmatrix}. \tag{87}$$

The quantities $\underline{\underline{W}} \cdot \underline{p}$, $\underline{\underline{D}} \cdot \underline{p}$ and $\underline{\underline{D}} : \underline{pp}$ are given by

$$\underline{\underline{W}} \cdot \underline{p} = W_{ij} p_j \hat{e}_i = W_{12} p_2 \hat{e}_1 + W_{21} p_1 \hat{e}_2, \tag{88}$$

$$\underline{\underline{D}} \cdot \underline{p} = D_{ij} p_j \hat{e}_i = D_{12} p_2 \hat{e}_1 + D_{21} p_1 \hat{e}_2, \tag{89}$$

$$\begin{aligned} \underline{\underline{D}} : \underline{pp} &= D_{ij}\hat{e}_i\hat{e}_j : p_k p_l \hat{e}_k \hat{e}_l \\ &= D_{11}p_1p_1 + D_{21}p_1p_2 + D_{31}p_1p_3 \ldots \\ &\quad + D_{12}p_2p_1 + D_{22}p_2p_2 + D_{32}p_2p_3 \ldots \\ &\quad + D_{13}p_3p_1 + D_{23}p_3p_2 + D_{33}p_3p_3 \\ &= D_{12}p_2p_1 + D_{21}p_1p_2. \end{aligned} \tag{90}$$

Thus, the governing equations for the fiber rotation in shear flow are given by

$$\frac{\mathrm{d}}{\mathrm{d}t}(p_1^{(i)}) = \frac{1}{2}\frac{\partial u}{\partial y} p_2^{(i)}[1 + \lambda(1 - 2p_1^{(i)}p_1^{(i)})] + \left(\frac{\mathrm{T}_{B,\perp 2}^{(i)}}{\xi_{\perp 2}^{(i)}} p_{\perp 1,1}^{(i)} - \frac{\mathrm{T}_{B,\perp 1}^{(i)}}{\xi_{\perp 1}^{(i)}} p_{\perp 2,1}^{(i)}\right), \tag{91}$$

$$\frac{\mathrm{d}}{\mathrm{d}t}(p_2^{(i)}) = \frac{1}{2}\frac{\partial u}{\partial y} p_1^{(i)}[-1 + \lambda(1 - 2p_2^{(i)}p_2^{(i)})] + \left(\frac{\mathrm{T}_{B,\perp 2}^{(i)}}{\xi_{\perp 2}^{(i)}} p_{\perp 1,2}^{(i)} - \frac{\mathrm{T}_{B,\perp 1}^{(i)}}{\xi_{\perp 1}^{(i)}} p_{\perp 2,2}^{(i)}\right), \tag{92}$$

$$\frac{\mathrm{d}}{\mathrm{d}t}(p_3^{(i)}) = -\lambda p_1^{(i)} p_2^{(i)} p_3^{(i)} \frac{\partial u}{\partial y} + \left(\frac{\mathrm{T}_{B,\perp 2}^{(i)}}{\xi_{\perp 2}^{(i)}} p_{\perp 1,3}^{(i)} - \frac{\mathrm{T}_{B,\perp 1}^{(i)}}{\xi_{\perp 1}^{(i)}} p_{\perp 2,3}^{(i)}\right). \tag{93}$$

References

Arnold, K., Hennrich, F., Krupke, R., Lebedkin, S., Kappes, M.M., 2006a. Length separation studies of single walled carbon nanotube dispersions. Physica Status Solidi B-Basic Solid State Physics 243 (13), 3073–3076.

Arnold, M.S., Green, A.A., Hulvat, J.F., Stupp, S.I., Hersam, M.C., 2006b. Sorting carbon nanotubes by electronic structure using density differentiation. Nature Nanotechnology 1 (1), 60–65.

Ausias, G., Fan, X.J., Tanner, R.I., 2006. Direct simulation for concentrated fibre suspensions in transient and steady state shear flows. Journal of Non-Newtonian Fluid Mechanics 135, 46–57.

Banerjee, S., Hemraj-Benny, T., Wong, S.S., 2005. Routes towards separating metallic and semiconducting nanotubes. Journal of Nanoscience and Nanotechnology 5 (6), 841–855.

Becker, M.L., Fagan, J.A., Gallant, N.D., Bauer, B.J., Bajpai, V., Hobbie, E.K., Lacerda, S.H., Migler, K.B., Jakupciak, J.P., 2007. Length-dependent uptake of DNA-wrapped single-walled carbon nanotubes. Advanced Materials 19, 939–945.

Butler, J.E., Shaqfeh, E.S.G., 2002. Dynamic simulations of the inhomogeneous sedimentation of rigid fibres. Journal of Fluid Mechanics 468, 205–237.

Butler, J.E., Shaqfeh, E.S.G., 2005. Brownian dynamics simulations of a flexible polymer chain which includes continuous resistance and multibody hydrodynamic interactions. Journal of Chemical Physics 122 (1).

Chattopadhyay, D., Lastella, S., Kim, S., Papadimitrakopoulos, F., 2002. Length separation of Zwitterion-functionalized single wall carbon nanotubes by GPC. Journal of the American Chemical Society 124 (5), 728–729.

Chattopadhyay, D., Galeska, L., Papadimitrakopoulos, F., 2003. A route for bulk separation of semiconducting from metallic single-wall carbon nanotubes. Journal of the American Chemical Society 125 (11), 3370–3375.

Chen, B.L., Selegue, J.P., 2002. Separation and characterization of single-walled and multiwalled carbon nanotubes by using flow field-flow fractionation. Analytical Chemistry 74 (18), 4774–4780.

Chen, Z., Du, X., Du, M.-H., Rancken, C.D., Hai-Ping Cheng, H.-P., Rinzler, A.G., 2003. Bulk separative enrichment in metallic or semiconducting single-walled carbon nanotubes. Nano Letters 3 (9), 1245–1249.

Chen, Z., Wu, Z.Y., Tong, L.M., Pan, H.P., Liu, Z.F., 2006. Simultaneous dielectrophoretic separation and assembly of single-walled carbon nanotubes on multigap nanoelectrodes and their thermal sensing properties. Analytical Chemistry 78 (23), 8069–8075.

Cobb, P.D., Byron, C., 2005. Simulations of concentrated suspensions of rigid fibers: relationship between short-time diffusivities and the long-time rotational diffusion. Journal of Chemical Physics 123, 054908-1–054908-19.

Cobb, P.D., Butler, J.E., 2006. Simulations of concentrated suspensions of semirigid fibers: Effect of bending on the rotational diffusivity. Macromolecules 39 (2), 886–892.

Dhont, J.K.G., van Bruggen, M.P.B., Briels, W.J., 1999. Long-time self-diffusion of rigid rods at low concentrations: a variational approach. Macromolecules 32 (11), 3809–3816.

Dhont, J.K.G., Briels, W.J., 2003. Viscoelasticity of suspensions of long, rigid rodds. Colloids and Surfaces A-Physicochemical and Engineering Aspects 213, 131–156.

Doorn, S.K., Strano, M.S., O'Connell, M.J., Haroz, E.H., Rialon, K.L., Hauge, R.H., Smalley, R.E., 2003. Capillary electrophoresis separations of bundled and individual carbon nanotubes. Journal of Physical Chemistry B 107 (25), 6063–6069.

Duesberg, G.S., Muster, J., Krstic, V., Burghard, M., Roth, S., 1998. Chromatographic size separation of single-wall carbon nanotubes. Applied Physics A-Materials Science & Processing 67 (1), 117–119.

Duesberg, G.S., Blau, W., Byrne, H.J., Muster, J., Burghard, M., Roth, S., 1999. Chromatography of carbon nanotubes. Synthetic Metals 103 (1–3), 2484–2485.

Farkas, E., Anderson, M.E., Chen, Z.H., Rinzler, A.G., 2002. Length sorting cut single wall carbon nanotubes by high performance liquid chromatography. Chemical Physics Letters 363 (1–2), 111–116.

Giddings, J.C., 1993. Field-flow fractionation – analysis of macromolecular, colloidal, and particulate materials. Science 260 (5113), 1456–1465.

Giddings, J.C., 2000. Field-Flow Fractionation Handbook. Wiley-Interscience.

Haddon, R.C., Sippel, J., Rinzler, A.G., Papadimitrakopoulos, F., 2004. Purification and separation of carbon nanotubes. MRS Bulletin 29 (4), 252–259.

Hennrich, F., Krupke, R., Kappes, M.M., Lohneysen, H.V., 2005. Frequency dependence of the dielectrophoretic separation of single-walled carbon nanotubes. Journal of Nanoscience and Nanotechnology 5 (7), 1166–1171.

Hsieh, C.C., Jain, S., Larson, R.G., 2006. Brownian dynamics simulations with stiff finitely extensible nonlinear elastic-Fraenkel springs as approximations to rods in bead-rod models. Journal of Chemical Physics 124 (4).

Huang, X.Y., McClean, R.S., Zheng, M., 2005. High-resolution length sorting and purification of DNA-wrapped carbon nanotubes by size-exclusion chromotography. Analytical Chemistry 77 (19), 6225–6228.

Janca, J., 1987. Field-Flow Fractionation. Marcel Dekker, New York.

Jeffery, G.B., 1922. The motion of ellipsoidal particles immersed in a viscous fluid. Proceedings of the Royal Society of London Series A 102, 161–179.

Kim, S., Karrila, S.J., 1991. Microhydrodynamics: Principles and Selected Applications. Butterworth-Heinemann, Stoneham.

Klaveness, E., Elgsaeter, A., 1999. Brownian dynamics of bead-rod-nugget-spring polymer chains with hydrodynamic interactions. Journal of Chemical Physics 110 (23), 11608–11615.

Krupke, R., Hennrich, F., v.Lohneysen, H., Kappes, M.M., 2003. Separation of metallic from semiconducting single-walled carbon nanotubes. Science 301, 344–347.

Krupke, R., Hennrich, F., 2005. Separation techniques for carbon nanotubes. Advanced Engineering Materials 7 (3), 111–116.

Liu, J., Rinzler, A.G., Dai, H.J., Hafner, J.H., Bradley, R.K., Boul, P.J., Lu, A., Iverson, T., Shelimov, K., Huffman, C.B., Rodriguez-Macias, F., Shon, Y.S., Lee, T.R., Colbert, D.T., Smalley, R.E., 1998. Fullerene pipes. Science 280 (5367), 1253–1256.

Mackaplow, M.B., Shaqfeh, E.S.G., 1996. A numerical study of the rheological properties of suspensions of rigid, non-Brownian fibres. Journal of Fluid Mechanics 329, 155–186.

Maeda, Y., Kimura, S., Kanda, M., Hirashima, Y., Hasegawa, T., Wakahara, T., Lian, Y.F., Nakahodo, T., Tsuchiya, T., Akasaka, T., Lu, J., Zhang, X.W., Gao, Z.X., Yu, Y.P., Nagase, S., Kazaoui, S., Minami, N., Shimizu, T., Tokumoto, H., Saito, R., 2005. Large-scale separation of metallic and semiconducting single-walled carbon nanotubes. Journal of the American Chemical Society 127 (29), 10287–10290.

Maeda, Y., Kanda, M., Hashimoto, M., Hasegawa, T., Kimura, S., Lian, Y.F., Wakahara, T., Akasaka, T., Kazaoui, S., Minami, N., Okazaki, T., Hayamizu, Y., Hata, K., Lu, J., Nagase, S., 2006. Dispersion and separation of small-diameter single-walled carbon nanotubes. Journal of the American Chemical Society 128 (37), 12239–12242.

Montesi, A., Morse, D.C., Pasquali, M., 2005. Brownian dynamics algorithm for bead-rod semiflexible chain with anisotropic friction. Journal of Chemical Physics 122 (8).

Moon, M.H., Kang, D.J., Jung, J.H., Kim, J.M., 2004. Separation of carbon nanotubes by frit inlet asymmetrical flow field-flow fractionation. Journal of Separation Science 27 (9), 710–717.

Peng, H.Q., Alvarez, N.T., Kittrell, C., Hauge, R.H., Schmidt, H.K., 2006. Dielectrophoresis field flow fractionation of single-walled carbon nanotubes. Journal of the American Chemical Society 128 (26), 8396–8397.

Perrin, F., 1936. Mouvement brownien d'un ellipsoïde: (II) Rotation libre et depolarisation des fluorescences. Translation et diffusion de molécules ellipsoïdales. Journal de Physique et le Radium 7, 1–11.

Ross, R.F., Klingenberg, D.J., 1998. Simulation of flowing wood fibre suspensions. Journal of Pulp and Paper Science 24 (12), 388–392.

Saintillan, D., Darve, E., Shaqfeh, E.S.G., 2005. A smooth particle-mesh Ewald algorithm for Stokes suspension simulations: The sedimentation of fibers. Physics of Fluids 17 (3).

Samsonidze, G.G., Chou, S.G., Santos, A.P., Brar, V.W., Dresselhaus, G., Dresselhaus, M.S., Selbst, A., Swan, A.K., Unlu, M.S., Goldberg, B.B., Chattopadhyay, D., Kim, S.N., Papadimitrakopoulos, F., 2004. Quantitative evaluation of the octadecylamine-assisted bulk separation of semiconducting and metallic single-wall carbon nanotubes by resonance Raman spectroscopy. Applied Physics Letters 85, 1006–1008.

Satoh, A., 2003. Introduction to Molecular-Microsimulation of Colloidal Dispersions. Elsevier Science B.V, Amsterdam, The Netherlands.

Schmid, C.F., Switzer, L.H., Klingenberg, D.J., 2000. Simulations of fiber flocculation: effects of fiber properties and interfiber friction. Journal of Rheology 44 (4), 781–809.

Schmid, C.F., Klingenberg, D.J., 2000a. Mechanical flocculation in flowing fiber suspensions. Physical Review Letters 84 (2), 290–293.

Schmid, C.F., Klingenberg, D.J., 2000b. Properties of fiber flocs with frictional and attractive interfiber forces. Journal of Colloid and Interface Science 226 (1), 136–144.

Selegue, J.P., Chen, B.L., Wijeratne, L., Meier, M.S., Wang, Z.W., Haddon, R.C., Hu, H., Andrews, R., 2001. Field-flow fractionation of single- and multi-walled carbon nanotubes. Abstracts of Papers of the American Chemical Society 222 U524.

Skjetne, P., Ross, R.F., Klingenberg, D.J., 1997. Simulation of single fiber dynamics. Journal of Chemical Physics 107 (6), 2108–2121.

Strano, M.S., Dyke, C.A., Usrey, M.L., Barone, P.W., Allen, M.J., Shan, H.C.K.C., Robert H. Hauge, R.H., Tour, J.M., Smalley, R.E., 2003. Electronic structure control of single-walled carbon nanotube functionalization. Science 301, 1519–1522.

Suarez, B., Simonet, B.M., Cardenas, S., Valcarcel, M., 2006. Separation of carbon nanotubes in aqueous medium by capillary electrophoresis. Journal of Chromatography A 1128 (1–2), 282–289.

Switzer, L.H., Klingenberg, D.J., 2003. Rheology of sheared flexible fiber suspensions via fiber-level simulations. Journal of Rheology 47 (3), 759–778.

Tagmatarchis, N., Zattoni, A., Reschiglian, P., Prato, M., 2005. Separation and purification of functionalised water-soluble rnulti-walled carbon nanotubes by flow field-flow fractionation. Carbon 43 (9), 1984–1989.

Tang, W.Z., Advani, S.G., 2005. Dynamic simulation of long flexible fibers in shear flow. CMES-Computer Modeling in Engineering & Sciences 8 (2), 165–176.

Tao, Y.G., den Otter, W.K., Briels, W.J., 2005a. Kayaking and wagging of rods in shear flow. Physical Review Letters 95 (23).

Tao, Y.G., den Otter, W.K., Padding, J.T., Dhont, J.K.G., Briels, W.J., 2005b. Brownian dynamics simulations of the self- and collective rotational diffusion coefficients of rigid long thin rods. Journal of Chemical Physics 122 (24).

Tao, Y.G., den Otter, W.K., Dhont, J.K.G., Briels, W.J., 2006. Isotropic-nematic spinodals of rigid long thin rodlike colloids by event-driven Brownian dynamics simulations. Journal of Chemical Physics 124 (13).

Toyoda, S., Yamaguchi, Y., Hiwatashi, M., Tomonari, Y., Murakami, H., Nakashima, N., 2007. Separation of semiconducting single-walled carbon nanotubes by using a long-alkyl-chain benzenediazonium compound. Chemistry-An Asian Journal 2 (1), 145–149.

Vetcher, A.A., Srinivasan, S., Vetcher, I.A., Abramov, S.M., Kozlov, M., Baughman, R.H., Levene, S.D., 2006. Fractionation of SWNT/nucleic acid complexes by agarose gel electrophoresis. Nanotechnology 17 (16), 4263–4269.

Yamamoto, S., Matsuoka, T., 1993. A method for dynamic simulation of rigid and flexible fibers in a flow field. Journal of Chemical Physics 98 (1), 644–650.

Yamamoto, S., Matsuoka, T., 1995a. Dynamic simulation of fiber suspensions in shear-flow. Journal of Chemical Physics 102 (5), 2254–2260.

Yamamoto, S., Matsuoka, T., 1995b. Dynamic simulation of flow-induced fiber fracture. Polymer Engineering and Science 35 (12), 1022–1030.

Yamamoto, S., Matsuoka, T., 1996. Dynamic simulation of microstructure and rheology of fiber suspensions. Polymer Engineering and Science 36 (19), 2396–2403.

Yamamoto, S., Matsuoka, T., 1997. Dynamic simulation of a platelike particle dispersed system. Journal of Chemical Physics 107 (8), 3300–3308.

Yang, Y.L., Xie, L.M., Chen, Z., Liu, M.H., Zhu, T., Liu, Z.F., 2005. Purification and length separation of single-walled carbon nanotubes using chromatographic method. Synthetic Metals 155 (3), 455–460.

Zheng, M., Jagota, A., Semke, E.D., Diner, B.A., Mclean, R.S., Lustig, S.R., Richardson, R.E., Tassi, N.G., 2003a. DNA-assisted dispersion and separation of carbon nanotubes. Nature Materials 2 (5), 338–342.

Zheng, M., Jagota, A., Strano, M.S., Santos, A.P., Paul Barone, P., Chou, S.G., Diner, B.A., Dresselhaus, M.S., Mclean, R.S., Onoa, G.B., Samsonidze, G.G., Semke, E.D., Usrey, M., Walls, D.J., 2003b. Structure-based carbon nanotube sorting by sequence-dependent DNA assembly. Science 302, 1545–1548.